

# A Comprehensive Study on Texture Development and Twin-Related Domain Evolution Following Hot Compression in a Super Austenitic Stainless Steel



K. ARUN BABU, C.N. ATHREYA, YAHYA H. MOZUMDER, V. SUBRAMANYA SARMA, and SUMANTRA MANDAL

Uniaxial hot deformation was carried out in a wide range of temperatures (1173 K to 1423 K) and strain rates (0.001 to 10 s<sup>-1</sup>) in a super austenitic stainless steel employing a Gleeble thermomechanical simulator. The evolution of fine grains due to dynamic recrystallization (DRX) with near-random texture was evident following deformation at strain rates 0.001 to 10 s<sup>-1</sup> and temperatures 1173 K to 1273 K. The deformed grains in this domain exhibited the typical formation of  $\langle 110 \rangle // \text{ND}$  or  $\alpha$  fiber, and its volume fraction gradually increased when the resistance to deformation increases. Weak deformation texture was persisted in the fine DRX grains ( $\leq 3 \mu\text{m}$ ) which gradually converted to a strong  $\langle 001 \rangle // \text{ND}$  fiber following grain growth. The deformation texture was simulated by employing a crystal plasticity finite element method (CPFEM). The texture inhomogeneity was observed in the typical compressed specimen which was associated with variation in stress/strain paths at different locations of the hot compressed specimen. Further, the  $\Sigma 3$  twin boundary evolution was analyzed employing Pande's relationship and twin-related domains (TRDs) analysis. The growth accident was identified as the major mechanism of  $\Sigma 3$  twin boundary evolution during DRX in this alloy. Moreover, the  $\Sigma 3$  regeneration was also evident in a small domain of hot working (1323 K/0.001 s<sup>-1</sup>) which was substantiated by texture randomization and formation of relatively larger TRDs in the microstructure.

<https://doi.org/10.1007/s11661-020-05763-8>

© The Minerals, Metals & Materials Society and ASM International 2020

## I. INTRODUCTION

SUPER austenitic stainless steels are widely used in various power plant and chemical industries due to its good combination of strength and corrosion resistance.<sup>[1-3]</sup> Hot deformation is employed to manufacture complex shapes and parts of the alloy which are extensively used in boilers and chemical pipelines.<sup>[4,5]</sup> Dynamic recrystallization (DRX) and dynamic recovery (DRV) are the two softening mechanisms that predominantly occur during hot deformation.<sup>[6-8]</sup> The occurrence of DRX during hot deformation has attracted attention as it plays a crucial role in microstructural evolution and grain refinement which eventually helps to reduce the forming load and optimize the mechanical

properties.<sup>[9-11]</sup> Nevertheless, the DRX kinetics is often complex as it is influenced greatly by processing parameters such as temperature, strain rate,<sup>[12,13]</sup> strain<sup>[14]</sup> in addition to state of stress,<sup>[15]</sup> initial microstructure,<sup>[16]</sup> and precipitation,<sup>[17]</sup> *etc.* Thus, a better understanding of the influence of processing parameters on the DRX behavior of super austenitic stainless steels is necessary to control microstructure during hot working.<sup>[18,19]</sup>

In addition to the evolution of strain-free grains, the grain boundary character distribution (GBCD) also changes during DRX.<sup>[6,20]</sup> Coincidence lattice boundaries (CSL) are a subset of high-angle boundaries and low  $\Sigma$  ( $\Sigma \leq 29$ ) CSL boundaries are believed to have unique properties.<sup>[21,22]</sup> In view of this, these boundaries are often separately analyzed to understand the GBCD evolution during thermomechanical processing.<sup>[21]</sup> Among CSL boundaries, the  $\Sigma 3$  annealing twin boundaries have gained great attention as these are found to play a key role in modifying GBCD<sup>[20,21]</sup> and controlling the kinetics of DRX.<sup>[20,23]</sup> It is well established that these  $\Sigma 3$  boundaries are generated during nucleation and growth of DRX grains,<sup>[20,23,24]</sup> though the exact mechanisms and their dependence on processing parameters

---

K. ARUN BABU, YAHYA H. MOZUMDER, and SUMANTRA MANDAL are with the Department of Metallurgical and Materials Engineering, Indian Institute of Technology Kharagpur 721302, India. Contact e-mail: arunbabuk@iitkgp.ac.in, arunbabuktkm@gmail.com C.N. ATHREYA and V. SUBRAMANYA SARMA are with the Department of Metallurgical and Materials Engineering, Indian Institute of Technology Madras, Chennai 600036, India.

Manuscript submitted December 10, 2019.

Article published online April 24, 2020

are not clear. Several researchers have pointed out that  $\Sigma 3$  twin boundary is generated due to growth accidents during strain-induced boundary migration (SIBM), and the twin density is dependent on the temperature and strain rates of deformation.<sup>[25–27]</sup> However, Pande's growth accident model has considered the variation of twin density as a function of grain size alone and not on temperature and strain rates.<sup>[28]</sup> Besides, it has been reported that the  $\Sigma 3$  twin boundaries could also form through  $\Sigma 3$  regeneration mechanism in addition to growth accident phenomenon.<sup>[20,21,29]</sup> During  $\Sigma 3$  regeneration, the  $\Sigma 3$  boundaries essentially interact with  $\Sigma 3$  or other higher order  $\Sigma 3$  boundaries to form a network of  $\Sigma 3^n$  (where  $n = 1, 2, 3, \text{ etc.}$ ) boundaries.<sup>[21]</sup> The cluster of grain boundaries characterized by  $\Sigma 3^n$  misorientation is generally termed as twin-related domains (TRDs).<sup>[30–32]</sup> It is well known that the formation of TRDs could effectively modify the grain boundary network, which could be helpful in improving mechanical<sup>[33]</sup> and corrosion properties<sup>[34,35]</sup> in materials. Nevertheless, limited research has been conducted to unravel the  $\Sigma 3$  regeneration, which could form large TRDs in the microstructure following hot working. Further, the implication of TRD formation on crystallographic texture development during hot deformation is also not much investigated in the past.

The flow behavior and DRX kinetics are also influenced by the crystallographic texture in the metals and alloys.<sup>[36]</sup> In a recent study, it has been reported that Goss texture retards the DRX kinetics and deteriorates mechanical properties in super austenitic stainless steels.<sup>[37]</sup> Several studies have reported the formation of  $\alpha$  fiber during hot deformation in austenitic stainless steels.<sup>[37–39]</sup> In fact, the evolution of crystallographic texture is dependent on various factors including the stacking fault energy,<sup>[40,41]</sup> crystal structure,<sup>[39]</sup> initial microstructure,<sup>[42]</sup> the extent of DRX,<sup>[36,38]</sup> *etc.* To predict the crystallographic texture effectively, several crystal plasticity models have been developed in the past.<sup>[43–46]</sup> These models have been incorporated into polycrystalline aggregate either as standalone programs<sup>[46–48]</sup> or incorporated into the commercial finite element software.<sup>[44,49]</sup> Amongst these models, the relaxed constrained model is defined by relaxing strain components whilst the stress components are maintained in equilibrium.<sup>[50]</sup> On the other hand, a full constrained model does not allow any strain relaxation, and the grain interaction is considered as extremely rigid.<sup>[50]</sup> Recently, a constrained hybrid model (which does not consider grain matrix interaction as completely rigid or completely relaxed), has been shown to predict the deformation texture with more accuracy.<sup>[43,45,49]</sup> Besides, finite element software has also been extensively used to study the texture evolution under various realistic boundary conditions.<sup>[49,51–53]</sup>

A comprehensive study on hot deformation behavior of a phosphorous modified super austenitic stainless steels has been reported recently.<sup>[2]</sup> However, a detailed study on microstructure, GBCD, and texture evolution following hot compression in this material is yet to be carried out. The present study is focused on understanding the microstructure and texture evolution in this

alloy following hot compression at various temperatures and strain rates (1173 K to 1423 K and 0.001 to 10 s<sup>-1</sup>). A crystal plasticity method is employed to predict the final deformation texture in a typical hot compressed specimen. The  $\Sigma 3$  twin boundary evolution is analyzed by employing TRD analysis and Pande's growth accident model, which is further corroborated with the DRX texture development in this alloy.

## II. EXPERIMENTAL AND SIMULATION DETAILS

### A. Material and Hot Compression Test

The chemical composition (in weight percentage) of super austenitic stainless steel employed in this study is summarized in Table I. The hot compression tests were performed in a cylindrical specimens with dimensions of 5 mm diameter and 8 mm length employing a thermo-mechanical simulator (Gleeble 3800). The specimens were deformed to a true strain of  $\sim 0.69$  at temperature varies from 1173 K to 1423 K (at 50 K interval), and strain rates ranging from 0.001 to 10 s<sup>-1</sup>.<sup>[2]</sup> Ni paste and graphite plates were inserted between specimen and platen to minimize friction. Following hot compression, the specimens were quenched with water in order to preserve the hot deformed microstructure. The load stroke data obtained from the thermomechanical simulator were converted to true stress and true strain data employing standard procedures.<sup>[54]</sup> Further, the flow curves obtained<sup>[2]</sup> were fitted using 9th order polynomials for smoothening the data.

### B. Microstructure Characterization

The hot compressed specimens were sectioned parallel to the compression axis (CA), in RD-ND plane (as shown in Figure 1) and polished using standard metallographic techniques. The orientation data were recorded from the maximum deformation zone of the hot compressed specimen (from the RD-ND plane) using an electron backscattered diffraction (EBSD) (EDAX-TSL Hikari EBSD detector) which is attached to a scanning electron microscope (INSPECT F<sup>®</sup> model, FEI, operating at 30 kV). The scans were performed at a step size of 0.5  $\mu\text{m}$  using hexagonal grids. Additionally, a high-resolution EBSD scan with a step size of 70 nm was also performed on the specimen compressed at 1173 K/10 s<sup>-1</sup> to evaluate the critical grain size for  $\Sigma 3$  twin boundary generation. The EBSD data were analyzed using TSL-OIM<sup>®</sup> software (version 7.2). The unindexed points were removed by the grain dilation single iteration approach. The deformed and recrystallized grains were identified employing grain orientation spread (GOS) criterion with a stipulation that grains with GOS < 1.5 deg are recrystallized grain.<sup>[2,19]</sup> The linear intercept method was employed to evaluate the average grain size of the as-received (AR) and hot deformed specimens. The grain sizes were measured considering twin boundaries and excluding twin boundaries from the analyses. Further, the average grain

**Table I. Composition (in Weight Percentage) of Super Austenitic Stainless Steel Used in This Study**

Ni	Cr	Mo	N	P	Mn	Cu	C	Fe
24.6	20.3	6.34	0.25	0.15	0.49	0.24	0.016	47.6

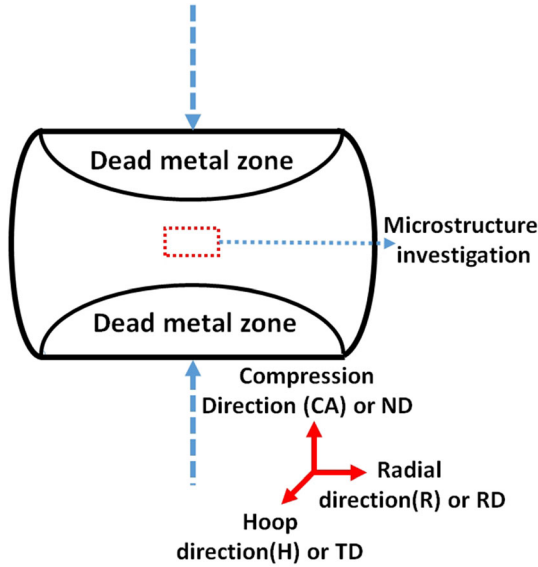


Fig. 1—Schematic illustration of the hot compressed specimen. The uniform (maximum) deformation zone wherein the microstructure investigation has been carried out is marked by a rectangle. The different directions are also marked.

diameter of DRX grain ( $D_{DRX}$ ) was also evaluated from the EBSD data. The boundaries with misorientation  $> 15$  deg have been considered as the high-angle boundaries (HABs). On the other hand, the random high-angle boundaries (RHABs) are the boundaries with misorientation  $> 15$  deg with a stipulation that they do not belong to low  $\Sigma$  ( $\leq 29$ ) misorientation. The length fraction of  $\Sigma 3$  boundaries ( $f_{\Sigma 3}$ ) was evaluated as  $\frac{L_{\Sigma 3}}{L_{HAB}}$  where  $L_{\Sigma 3}$  and  $L_{HAB}$  is the total boundary length of  $\Sigma 3$  boundaries and HABs, respectively. Similarly, the sum of the boundary length fraction of  $\Sigma 9$  and  $\Sigma 27$  boundaries ( $f_{\Sigma 9+\Sigma 27}$ ) was evaluated as  $\frac{L_{\Sigma 9+\Sigma 27}}{L_{HAB}}$  where  $L_{\Sigma 9}$  and  $L_{\Sigma 27}$  is the total boundary length of the  $\Sigma 9$  and  $\Sigma 27$  boundaries, respectively. The  $\Sigma 3$  twin density (TD) ( $1/\mu\text{m}$ ) was also evaluated from the EBSD maps employing the following equation,<sup>[55]</sup>

$$TD = \left(\frac{2}{\pi}\right) \left(\frac{L_{\Sigma 3}}{S}\right) \quad [1]$$

where  $s$  is the total surface area of the microstructure examined. In this study, TRD analyses were performed using ARPGE software.<sup>[56]</sup> ARPGE software identifies the grains related by  $\Sigma 3^n$  ( $n \leq 3$ ) boundaries and

assigns these grains to a particular TRD. Each TRDs in the microstructure may contain multiple grains and the average values of the number of grains present per TRD were calculated. The ARPGE software also evaluates the length of the longest twin chain (LLC) for a particular TRD by creating TRD trees.<sup>[56]</sup> Essentially, LLC represents the twinning order (or  $n$  associated with a  $\Sigma 3^n$  boundary) of the TRD.<sup>[30]</sup>

### C. Texture Characterization

The EBSD scans, which were initially taken from RD-ND plane, rotated in such a way that the normal to the EBSD scan (in TD axis) coincides with the compression axis (ND axis) (see Figure 1). Minimum 5000 grains in each hot deformation condition were considered for the evaluation of the crystallographic texture in the present study. Orientation distribution function (ODF) was evaluated based on a ‘series harmonic expansion method’ applying triclinic sample symmetry employing MTEX 5.2.3 toolbox which runs in Matlab<sup>®</sup> 2016. The volume fraction of different fiber components were directly evaluated from EBSD data by applying 15 deg tolerance with the help of TSL-OIM<sup>®</sup> software. The texture strength is expressed as the multiples of random density (MRD)<sup>[38]</sup> where MRD = 1 represents the random distribution, and a higher MRD value represents an increase in the strength of the texture.

### D. Crystal Plasticity Simulation

The deformation texture was simulated employing the crystal plasticity finite element method (CPFEM). The simulation was performed using a commercial finite element software Abaqus 6.14 equipped with a user material subroutine (UMAT) code. The model has been meshed with 3D, 8 node continuum elements with reduced integration (or C3D8R elements in Abaqus 6.14<sup>®</sup>).

#### 1. Theory

In the present study, the octahedral slip systems ( $\{111\} \langle 110 \rangle$  slip) were used which are usually employed to predict the deformation texture in low to medium SFE FCC materials.<sup>[46,49,50,57]</sup> The FCC materials deform via crystallographic slip on twelve  $\{111\} \langle 110 \rangle$  slip systems if the resolved stress is higher than the critical resolved shear stress.<sup>[51]</sup> The resolved shear strain rate ( $\dot{\gamma}^\alpha$ ) on each slip system ( $\alpha$ ) could be expressed as,<sup>[49]</sup>

$$\dot{\gamma}^\alpha = \dot{\gamma}_o \left| \frac{\tau^\alpha}{k^\alpha} \right|^{\frac{1}{m}} \text{sgn}(\tau^\alpha) \quad [2]$$

where  $\tau^\alpha$  is the resolved shear stress,  $k^\alpha$  is the slip system strength,  $\dot{\gamma}_o$  is the reference shear strain rate, and  $m$  is the strain rate sensitivity. The  $\tau^\alpha$  was evaluated based on deviatoric stress tensor ( $\sigma_d$ ) and Schmid tensor ( $s^\alpha \otimes n^\alpha$ ) (where  $s^\alpha$  and  $n^\alpha$  are slip direction and slip plane normal, respectively) as follows,<sup>[49]</sup>

$$\tau^\alpha = \sigma_d : s^\alpha \otimes n^\alpha \quad [3]$$

Further, the rate of hardening  $\left(\frac{dk^z}{dt}\right)$  on each slip system could be further expressed based on a modified Voce law<sup>[45]</sup> given as,

$$\frac{dk^z}{dt} = h_0^z \left( 1 - \left( \frac{k^z - k_0^z}{\tau_s^z - k_0^z} \right) \right) \sum_1^N \dot{\gamma}^z \quad [4]$$

where  $h_0^z$  is the initial hardening rate,  $k_0^z$  is the initial yield stress,  $\tau_s^z$  is the saturation stress and  $N$  is the total number of available slip systems. The resolved shear stress ( $\tau^z$ ) on each slip system ( $z$ ) could be expressed<sup>[49]</sup> as,

$$\tau_s^z = \tau_{so}^z \left| \frac{\dot{\gamma}^z}{\dot{\gamma}_{so}^z} \right|^{m'} \quad [5]$$

where  $\tau_{so}^z$ ,  $\dot{\gamma}_{so}^z$  and  $m'$  are constants. The aggregate responses of the polycrystal were computed using extended Taylor's hypothesis wherein each crystal is assumed to deform identically and all the slip systems harden at the same rate.<sup>[49]</sup> Hence, the constants are assumed to be slip system-independent ( $h_0^z \rightarrow h_0$ ,  $k_0^z \rightarrow k_0$ ,  $\tau_{so}^z \rightarrow \tau_{so}$  and  $\dot{\gamma}_{so}^z \rightarrow \dot{\gamma}_{so}$ ). The constants were identified from experimental flow curves corresponding to the temperature 1173 K and strain rate 0.001 to 10 s<sup>-1</sup>. The constants accurately represent the material behavior<sup>[58]</sup> since the work hardening part of the simulated flow curves yielded a good correlation with experimental flow curves (Figure 2(a)). Such a method for the evaluation of simulation constants from the experimental flow curves could be referred to as the 'inverse modeling approach'.<sup>[58]</sup> Moreover, the flow curves (0.001 to 0.1 s<sup>-1</sup>, Figure 2(a)) revealed some flow softening after peak stress which is attributed to DRX and this portion was avoided to evaluate CPFEM constants. The constants employed for the CPFEM simulation at various strain rates are given in Table II.

### III. RESULTS

#### A. Flow Behavior and Microstructure Evolution

Flow stress increased during the initial stages of the deformation until it reaches distinct peak stress, which is evident in all the representative flow curves, as illustrated in Figure 2(b). Figure 3(a) shows the inverse pole figure (IPF) map of the AR specimen consisting of homogeneous and near equiaxed grains (grain size  $\sim 13.4 \pm 1 \mu\text{m}$  (with twin boundaries) or  $22.5 \pm 1.4 \mu\text{m}$  (without twin boundaries)). The corresponding misorientation distribution plot is shown in Figure 4(a). Analysis of grains with GOS < 1.5 deg shows that the AR microstructure was almost fully ( $\sim 95$  pct) recrystallized. The misorientation distribution plot reveals that the  $\sum 3$  boundaries which are identified by 60 deg  $\langle 111 \rangle$  misorientation, constituted a large proportion of HABs (Figure 4(a)) in the AR microstructure.

The IPF maps of the specimens compressed at different temperatures and strain rates (see Figures 3(b) through (h)) reveal that the microstructural attributes such as grain size and grain morphology vary significantly with the processing conditions. The grain sizes (with twin boundaries) in different conditions were quantified and shown in Figure 5(a). The specimen compressed at 1173 K to 1273 K/1 to 10 s<sup>-1</sup> (see Figures 3(b) and (c)) indicates low DRX fraction (< 25 pct, see Figure 5(b)). The representative microstructure in this regime indicates the presence of small DRX grains ( $\leq 3 \mu\text{m}$ , Figure 5(a) and Figures 3(b) and (c)) which were predominantly nucleated at grain boundaries thus forming a typical 'necklace'<sup>[6]</sup> type of microstructure. Further, the specimen compressed at 1273 K/0.1 s<sup>-1</sup> (see Figure 3(d)) characterized by the coexistence of moderate fraction of recrystallized ( $X_{\text{DRX}} \sim 40$  pct, Figure 5(b)) and deformed grains. Misorientation distribution plot

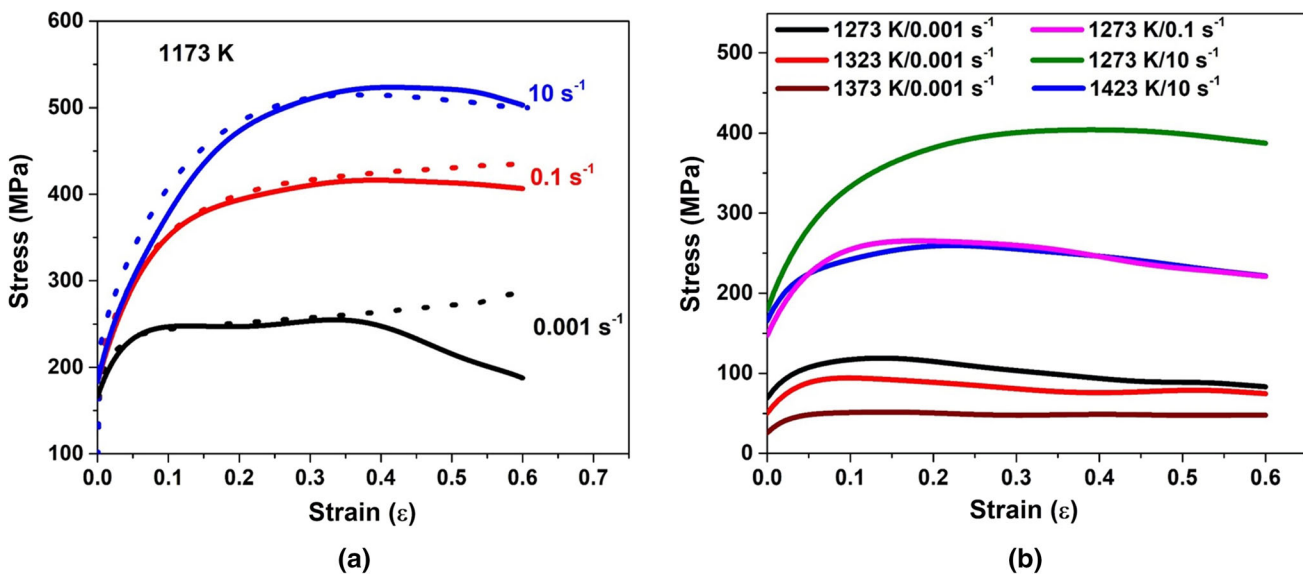


Fig. 2—The stress ( $\sigma$ )—strain ( $\epsilon$ ) plots of super austenitic stainless steel following hot compression (a) at 1173 K and 0.001 to 10 s<sup>-1</sup> (in thick solid line) which is superimposed with simulated flow curves (in dotted line); (b) at different temperatures and strain rates (the hot compression conditions are shown in legends). The experimental flow stress data have been taken from Ref. [2].

Table II. The Constants Employed for CPFEM Simulation

	C11 (GPa)	C12 (GPa)	C44 (GPa)	$h_o$ (MPa)	$k_o$ (MPa)	$\tau_{so}$ (MPa)	$\dot{\gamma}$	$m$	$m'$
$0.001 \text{ s}^{-1}$	168	72	48	300	75	98	$5 \times 10^{10}$	0.27	$5 \times 10^{-4}$
$0.1 \text{ s}^{-1}$	168	72	48	300	75	145	$5 \times 10^{10}$	0.11	$5 \times 10^{-4}$
$10 \text{ s}^{-1}$	168	72	48	300	75	173	$5 \times 10^{10}$	0.0025	$5 \times 10^{-4}$

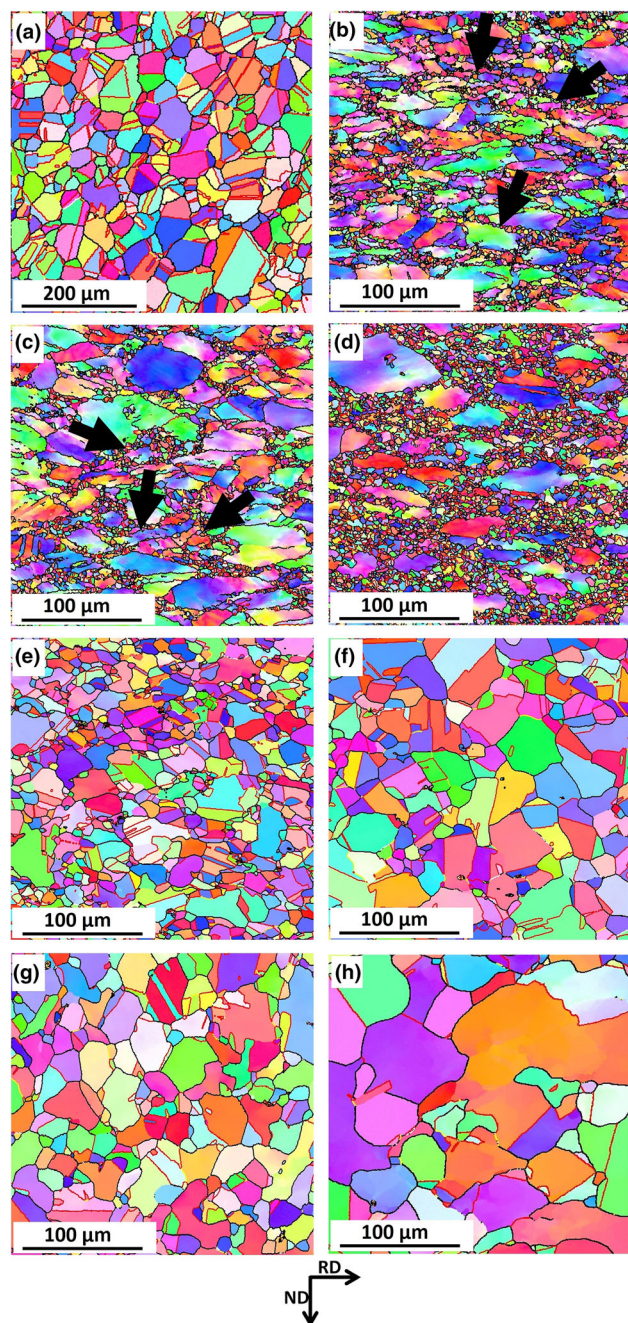


Fig. 3—IPF map of the (a) as-received as well as following hot deformation at (b) 1223 K and  $10 \text{ s}^{-1}$ , (c) 1273 K and  $10 \text{ s}^{-1}$ , (d) 1273 K and  $0.1 \text{ s}^{-1}$ , (e) 1273 K and  $0.001 \text{ s}^{-1}$ , (f) 1323 K and  $0.001 \text{ s}^{-1}$ , (g) 1423 K and  $0.1 \text{ s}^{-1}$ , and (h) 1373 K and  $0.001 \text{ s}^{-1}$ . The necklace portion of the microstructure is indicated by thick solid arrows in (f through g). (boundary color code, HAB: black,  $\Sigma 3$ : Red,  $\Sigma 9$ : yellow,  $\Sigma 27$ : white) (Color figure online).

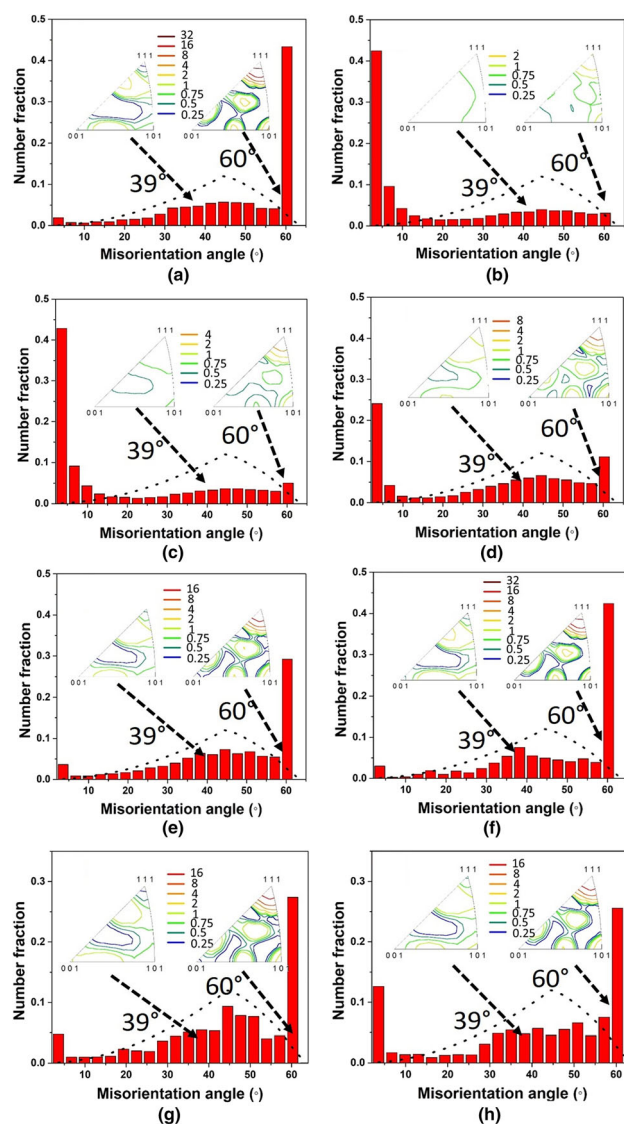


Fig. 4—The misorientation distribution of the (a) as-received specimen, as well as following hot deformation at (b) 1223 K and  $10 \text{ s}^{-1}$ , (c) 1273 K and  $10 \text{ s}^{-1}$ , (d) 1273 K and  $0.1 \text{ s}^{-1}$ , (e) 1273 K and  $0.001 \text{ s}^{-1}$ , (f) 1323 K and  $0.001 \text{ s}^{-1}$ , (g) 1423 K and  $0.1 \text{ s}^{-1}$ , and (h) 1373 K and  $0.001 \text{ s}^{-1}$ . Dotted distribution indicates Mackenzie distribution. The misorientation axis distribution corresponding to the 60 deg and 39 deg misorientation angles is represented in standard stereographic triangles.

reveals that the fraction of sub-boundaries was increased at low DRX regime (Figures 4(b) through (d)). The  $\Sigma 3$  boundary fraction decreased at low DRX regime which is due to the loss of twin orientation (deviated from its ideal 60 deg  $\langle 111 \rangle$  misorientation) during deformation.<sup>[36]</sup>

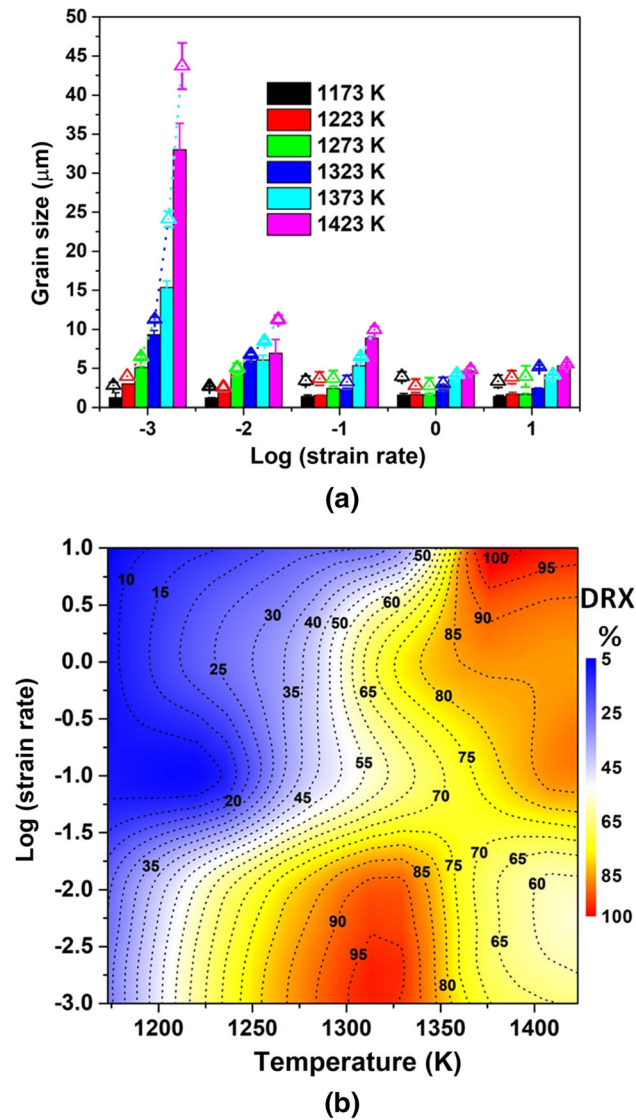


Fig. 5—The variation of (a) grain diameter of DRX grain (illustrated as a bar chart) and the average grain size (indicated by triangles connected by dotted lines), (b) DRX fraction with respect to temperatures and strain rates in the range of 1173 K to 1423 K and 0.001 to  $10 \text{ s}^{-1}$ .

The microstructures corresponding to the specimens hot compressed at 1273 K to 1323 K/ $0.001 \text{ s}^{-1}$  (Figures 3e through (f)) reveal equiaxed and fine DRX grains ( $\sim 7$  to  $12 \mu\text{m}$  with twin boundaries, see Figure 5(a) or  $9$  to  $20 \mu\text{m}$  without twin boundaries) with a high DRX fraction ( $X_{\text{DRX}} > 85$  pct, Figure 5(b)). The flow curves show significant flow softening due to the occurrence of high DRX activity (Figure 2(b)). Similarly, the representative microstructure (Figure 3(g)) corresponding to the temperatures and strain rates of  $\sim 1373 \text{ K}$  to  $1423 \text{ K}/0.1$  to  $10 \text{ s}^{-1}$  also reveals the presence of fine and equiaxed DRX grains ( $\sim 4$  to  $10 \mu\text{m}$  with twin boundaries, Figure 5(a) or  $6$  to  $13 \mu\text{m}$  without twin boundaries) with a significant DRX fraction ( $X_{\text{DRX}} > 85$  pct, Figure 5(b)). The misorientation distribution plots of these conditions reveal very low fraction of sub-boundaries (see

Figures 4(e) through (g)). Further, the misorientation distribution of the specimen deformed at 1323 K/ $0.001 \text{ s}^{-1}$  shows a clear peak at  $60 \text{ deg } \langle 111 \rangle$  and  $39 \text{ deg } \langle 110 \rangle$  positions (Figure 4(f)) which are associated with the formation of  $\Sigma 3$  and  $\Sigma 9$  boundaries, respectively. The deformation at temperature 1423 K and strain rate  $0.001 \text{ s}^{-1}$  is characterized by the significant grain coarsening ( $\sim 43 \mu\text{m}$  with twin boundaries, Figure 5(a) and Figure 3(h) or  $50 \mu\text{m}$  without twin boundaries). The misorientation distribution plot in this specimen also shows significant fraction of  $\Sigma 3$  boundaries (Figure 4(h)).

## B. Grain Boundary Character Distribution

The variation of the length fraction of  $\Sigma 3$  boundaries (i.e.,  $f_{\Sigma 3}$ ) at different temperatures and strain rates is illustrated in Figure 6. It is evident that the  $f_{\Sigma 3}$  increased with the increasing DRX fraction (Figures 6 and 5(b)) in the range of temperatures and strain rates studied in the present work. A maximum value of  $f_{\Sigma 3}$  is obtained at the conditions viz.  $1323 \text{ K}/0.001 \text{ s}^{-1}$  and  $1373 \text{ K}$  to  $1423 \text{ K}/10 \text{ s}^{-1}$ . Further, the variation of the sum of the fractions of  $\Sigma 9$  and  $\Sigma 27$  boundaries (i.e.,  $f_{\Sigma 9+\Sigma 27}$ ) is also shown in Figure 6. The  $f_{\Sigma 9+\Sigma 27}$  was relatively higher at the condition  $1323 \text{ K}/0.001 \text{ s}^{-1}$ , and a further increase in the strain rate or temperature resulted in the decrease of the  $f_{\Sigma 9+\Sigma 27}$  following deformation (Figure 6).

The variation of  $f_{\Sigma 3}$  is plotted against DRX grain size ( $D_{\text{DRX}}$ ), as illustrated in Figure 7. It is observed that  $f_{\Sigma 3}$  followed an exponential relationship with  $D_{\text{DRX}}$  given as,<sup>[25]</sup>

$$f_{\Sigma 3} = F \left\{ 1 - \exp \left( \frac{\beta' D_{\text{DRX}}}{D_0} \right) \right\} \quad [6]$$

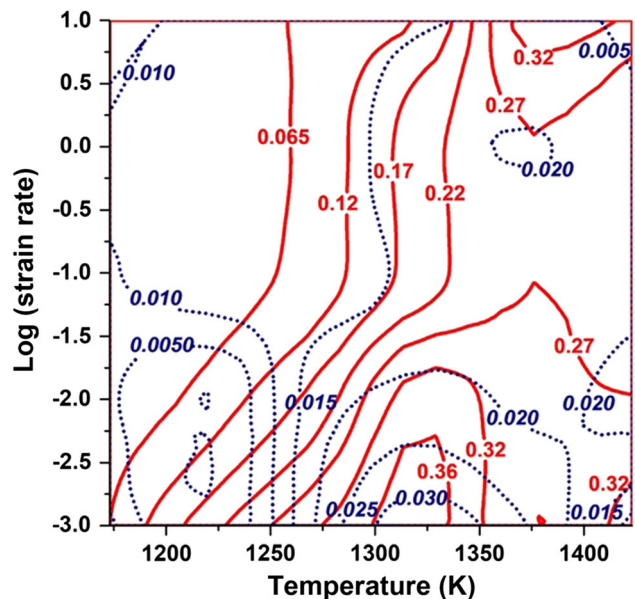


Fig. 6—The variation of  $f_{\Sigma 3}$  (in thick red line) and  $f_{\Sigma 9+\Sigma 27}$  (in blue dotted line) with respect to strain rate (in log scale) ( $0.001$  to  $10 \text{ s}^{-1}$ ) and temperature ( $1173 \text{ K}$  to  $1423 \text{ K}$ ) (Color figure online).

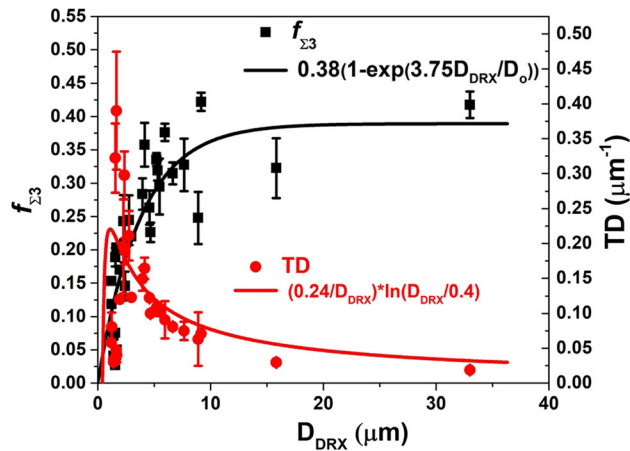


Fig. 7—The variation of  $f_{\Sigma 3}$  and twin density (TD) with respect to grain diameter of DRX grain ( $D_{\text{DRX}}$ ) in the temperature range 1173 K to 1423 K and strain rate range 0.001 to  $10 \text{ s}^{-1}$ . The TD is fitted (shown by red lines) employing Pande's relationship (see Eq. [7]) (Color figure online).

here  $D_o$  is the grain size ( $\sim 13.4 \mu\text{m}$ ) in the AR specimen,  $F$  is a proportionality constant ( $\sim 0.38$ ) and  $\beta'$  is a constant ( $\sim 3.75$ ). Here, the  $\Sigma 3$  twin boundary fraction increased significantly with the increase in grain size up to a critical limit. Further increase in grain size does not seem to change the fraction of  $\Sigma 3$  boundaries significantly (Figure 7).

The variation of TD with DRX grain size could be explained based on Pande's relationship<sup>[28]</sup> given as,

$$\text{TD} = \frac{k}{D_{\text{DRX}} \ln \left( \frac{D_{\text{DRX}}}{D_c} \right)} \quad [7]$$

The variation of TD is plotted against grain size, and the data points are fitted with Eq. [7], as illustrated in Figure 7. It is observed that the fit in Figure 7 almost followed Eq. [7] thus, it is possible to conclude that the material under investigation essentially obeys Pande's relationship.<sup>[28]</sup> Here,  $D_c$  is the critical grain size required for the twin generation.<sup>[29,59]</sup> The critical grain diameter (obtained as  $\sim 0.4 \mu\text{m}$ ) was evaluated from a high-resolution EBSD scan (see Figure 8). The value is consistent with the reported values of the critical grain sizes in metals and alloys, which varies between 0.1 and  $2.5 \mu\text{m}$ .<sup>[25]</sup>

The formation of TRDs following hot deformation was evaluated employing different statistical parameters, *i.e.*, number of grains per TRD ( $N_{\text{TRD}}$ ) and length of the longest chain (LLC). The parameter  $N_{\text{TRD}}$  refers to the average number of grains present within a TRD network.<sup>[32,56]</sup> On the other hand, the LLC reveals the maximum order of the twinning present in a TRD network.<sup>[32,56]</sup> The average  $N_{\text{TRD}}$  and LLC in the AR specimen were evaluated to be 0.8 and 5.2, respectively. These typical values of  $N_{\text{TRD}}$  and LLC also indicate the presence of relatively larger TRDs and multiple twinning in the AR microstructures.<sup>[30–32]</sup> Further, the average LLC and  $N_{\text{TRD}}$  were evaluated for the entire range of processing conditions and shown in Figure 9. It

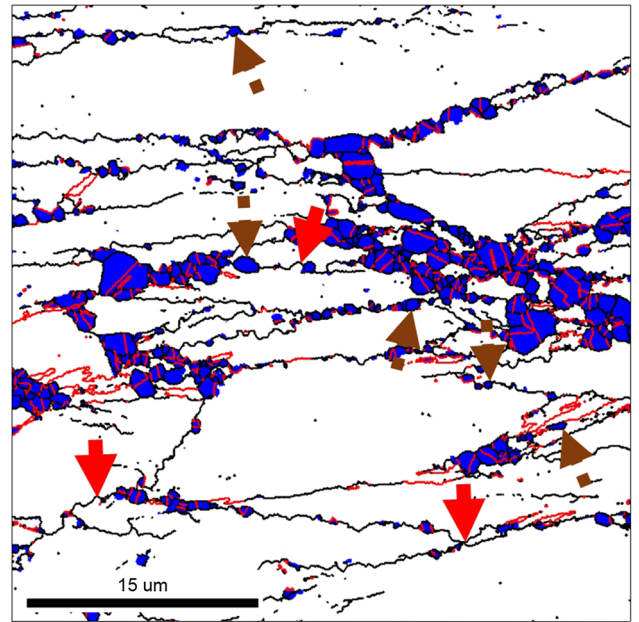


Fig. 8—The grain boundary map superimposed with color-coded grains corresponding to the temperature 1173 K and strain rate  $10 \text{ s}^{-1}$ . The blue-colored region represents the recrystallized grains whereas the white-colored region corresponds to the deformed grains. The boundaries which do not contain any  $\Sigma 3$  boundaries are indicated by brown dotted arrows, and the bulged boundaries are marked by solid red arrows (boundary color code: HAB-black,  $\Sigma 3$ -red) (Color figure online).

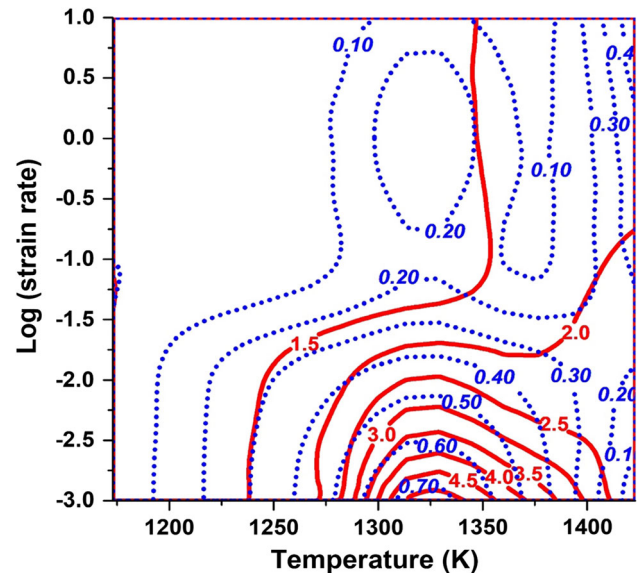


Fig. 9—The variation of number of grain per TRD, or  $N_{\text{TRD}}$  (in thick red lines) and average LLC (in blue dotted line) with respect to strain rate (in log scale) ( $0.001$  to  $10 \text{ s}^{-1}$ ) and temperature (1173 K to 1423 K) (Color figure online).

is observed that the average LLC ( $\leq 0.4$ ) and  $N_{\text{TRD}}$  ( $< 2$ ) values were very low in strain rates and temperatures of  $0.001$  to  $0.01 \text{ s}^{-1}$ /1173 K to 1223 K and  $0.01$  to  $10 \text{ s}^{-1}$ /1173 K to 1323 K (Figure 9). The decrease in  $N_{\text{TRD}}$  as compared to AR specimen indicates the absence of multiple twinning in this domain.<sup>[30–32]</sup> The

low value of average LLC also corresponds to the limited number of twinned grains in the domain.<sup>[30–32]</sup> The TRD networks, as observed in the AR condition (Figure 10(a)), were disrupted in these deformation condition and each deformed grains contains several such TRD clusters (each TRD is identified by separate colors) (Figures 10(b) through (d)). This phenomenon is due to the loss of twin orientation and the formation of large fraction of sub-boundaries (see Figures 4(b) through (d)) during deformation which leads to the

disruption of the TRD network present in the AR specimen. Following deformation at 1273 K to 1373 K/0.001 to 0.01 s<sup>-1</sup>, the average LLC (0.4 to 0.7) and N<sub>TRD</sub> (2 to 5) values were marginally increased (Figure 9). This is also manifested in the size of the TRDs as shown in Figures 10(e) through (f). While the size of TRDs increased during grain growth at high temperature and low strain rates (1373 K/0.001 s<sup>-1</sup>) as illustrated in Figure 10(g), the N<sub>TRD</sub> (< 3.5) and average LLC (~ 0.4) values were found to be decreased (Figure 9). On the other hand, the TRD size appears to be reduced (Figure 10(f)) following deformation at medium to high strain rates (*i.e.*, 1423 K/0.1 s<sup>-1</sup>). The N<sub>TRD</sub> (≤ 2) and average LLC (≤ 0.4) values were also low in this domain (Figure 9).

### C. Texture Evolution

The important texture components obtained from  $\varphi_2 = 0$  deg and  $\varphi_2 = 45$  deg sections of ODFs are illustrated in Figure 11(a). The AR specimen is characterized by a near-random texture (MRD ~ 1.8, Figure 11(b)) whilst relatively weak near {120} <001> and near Brass components (and its symmetric variants) is evident in ODF sections (Figures 11(a) and (b)). The texture evolution in deformed grains (*i.e.*, GOS ≥ 1.5 deg) (Figure 11(c)) and DRX grains (GOS < 1.5 deg) (Figures 11(d) through (k)) following hot deformation are discussed in the following sections.

#### 1. Texture evolution in deformed grains

The  $\varphi_2 = 0$  deg and  $\varphi_2 = 45$  deg sections of the ODFs evaluated from the deformed (grains with GOS ≥ 1.5 deg) grains following deformation at 1173 K/10 s<sup>-1</sup> is presented in Figure 11(c). The deformed grains show significant texture strengthening (MRD ~ 3.5, see Figure 11(c)) as compared to the AR condition (Figure 11(b)). The deformation texture composed of near Goss ( $\varphi_1 = 180$  deg,  $\phi = 45$  deg,  $\varphi_2 = 0$  deg, MRD ~ 2.9), and near Brass ( $\varphi_1 = 145$  deg,  $\phi = 45$  deg,  $\varphi_2 = 0$  deg, MRD ~ 3.1) ideal orientations (see Figures 11(a) and (c)) shown in the  $\varphi_2 = 0$  deg section. These orientations were typically located in <011>//ND fiber (for FCC rolling, it is  $\alpha$  fiber), which could be identified from ND-IPF as shown in Figure 12(a) (MRD ~ 2.6). Other deformation fibers such as <111>//RD and <001>//RD are (Figure 12(a), MRD ~ 1.4) also evident in RD-IPF following compression. These components are typically associated with Goss and {110} <111> type texture which is stable during hot compression. It is observed that the texture intensity of <011>//ND fiber in deformed grains increased following deformation at high strain rates (Figure 13(a)). While the texture intensity of  $\beta$  fiber progressively increased from Copper {112} <111> through S {123} <634> and reaches the maximum at Brass orientation (Figure 13(b)), it is found to be weakly dependent on strain rate. It is noted that the intensity of the Brass component (which lies in both  $\alpha$  and  $\beta$  fibers) also increased with the strain rate (Figures 13(a) and (b)). The  $\tau$  fiber refers to <011>//TD fiber component,<sup>[39]</sup> and it shows a gradual increase in the texture intensity from

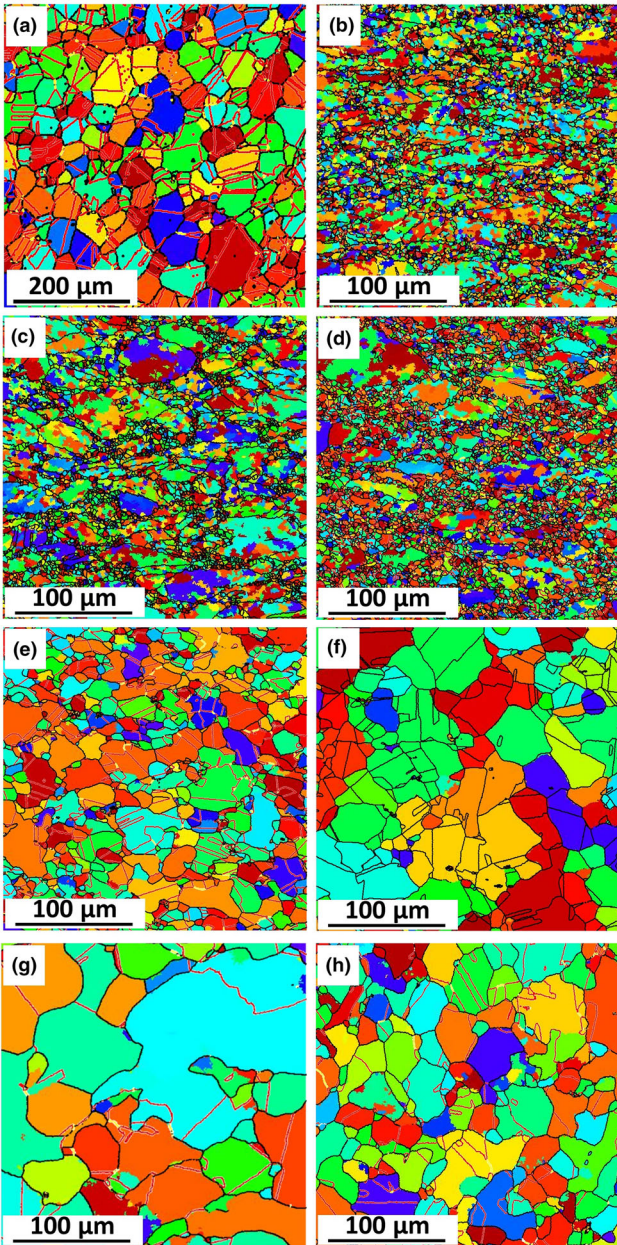


Fig. 10—TRD reconstructed map superimposed with grain boundaries of the (a) as-received, as well as following hot deformation at (b) 1223 K and 10 s<sup>-1</sup>, (c) 1273 K and 10 s<sup>-1</sup>, (d) 1273 K and 0.1 s<sup>-1</sup>, (e) 1273 and 0.001 s<sup>-1</sup>, (f) 1323 K and 0.001 s<sup>-1</sup>, (g) 1373 K and 0.001 s<sup>-1</sup>, and (h) 1423 K and 0.1 s<sup>-1</sup>. Different TRDs are indicated by different colors (Boundary color code, HAB: black, Σ3: Red, Σ9: yellow, Σ27: white) (Color figure online).



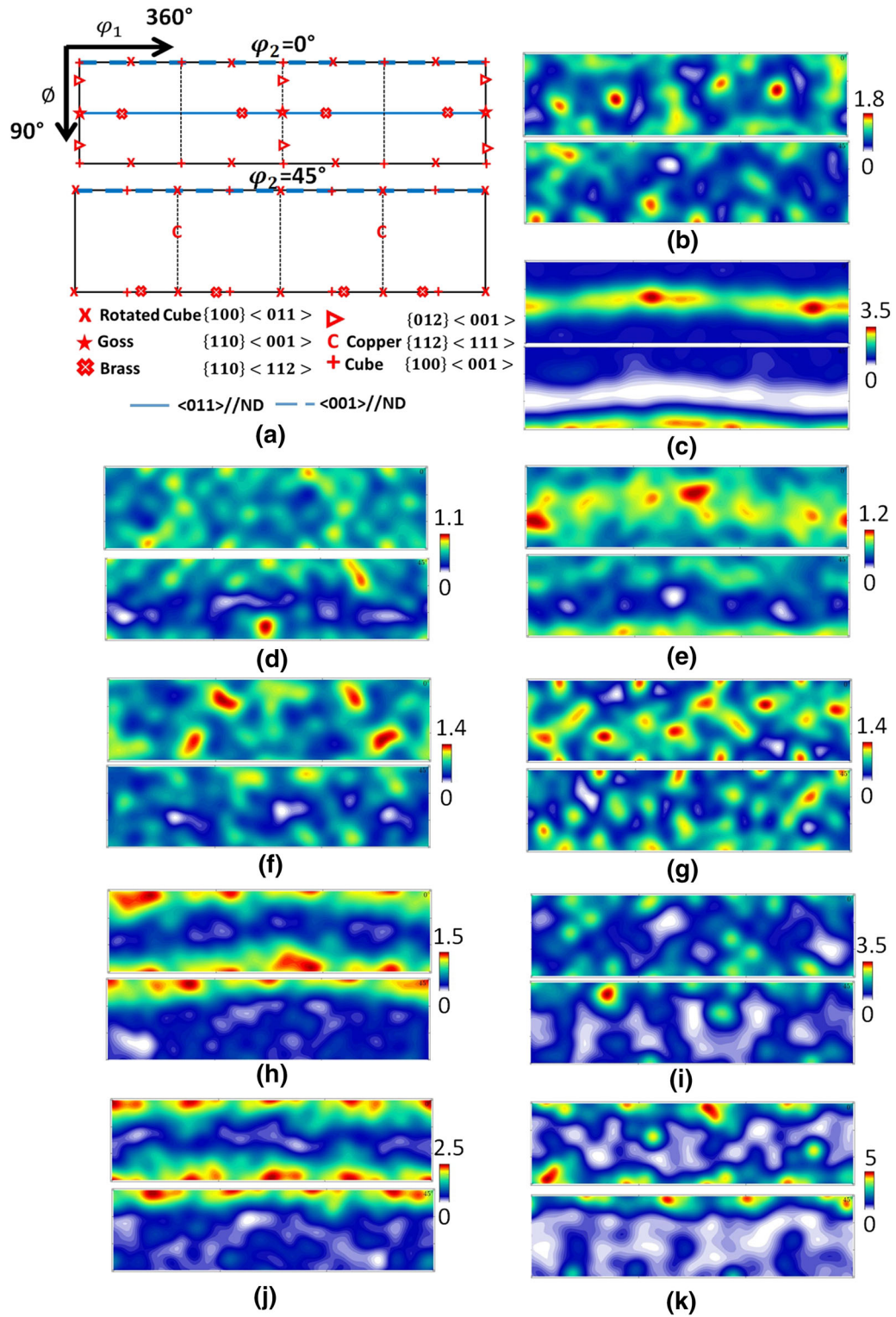


Fig. 11—(a) Orientation distribution function (ODF) showing  $\phi_2 = 0$  deg and  $\phi_2 = 45$  deg sections to illustrate the ideal rolling texture components for FCC materials. The ODF in (b) as-received, as well as specimen deformed at (c and d) 1173 K and  $10 \text{ s}^{-1}$ , (e) 1273 K and  $0.1 \text{ s}^{-1}$ , (f) 1273 K and  $0.001 \text{ s}^{-1}$ , (g) 1323 K and  $0.001 \text{ s}^{-1}$ , (h) 1423 K and  $10 \text{ s}^{-1}$ , (i) 1373 K and  $0.001 \text{ s}^{-1}$ , (j) 1423 K and  $0.1 \text{ s}^{-1}$ , and (k) 1423 K and  $0.001 \text{ s}^{-1}$  is also shown. The ODF section in (c) is evaluated from deformed grains whereas the same in (b) as well as (d through k) is evaluated from DRX grains.

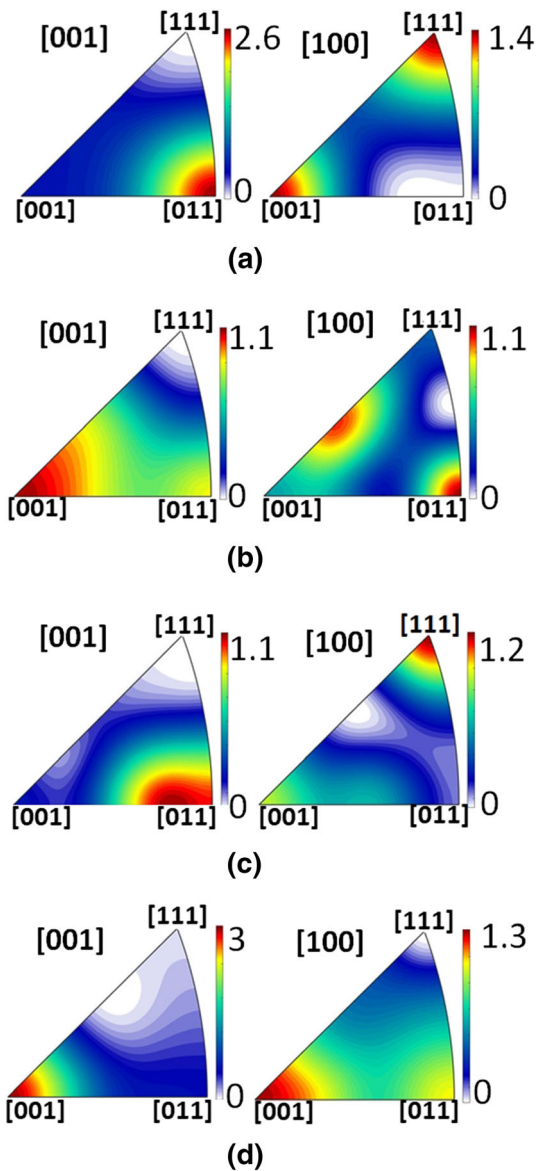


Fig. 12—The ND or [001] and RD or [100] inverse pole figure (IPF) of the specimen deformed at (a and b) 1173 K and  $10 \text{ s}^{-1}$ , (c) 1323 K and  $0.001 \text{ s}^{-1}$ , and (d) 1423 K and  $0.001 \text{ s}^{-1}$ . The IPF shown in (a) is evaluated from the deformed grains whereas (b) through d) is evaluated from the DRX grains.

Copper to Goss orientations following deformation (Figure 13(c)). An increase in the texture intensity of Goss orientation with strain rate is also evident (Figure 13(c)).

### 2. Crystal plasticity simulation in deformed grains

The schematic illustration of the compression specimen meshed with C3D8R-type elements is shown in Figure 14(a). The typical RD-ND section hot compressed specimen is illustrated in Figure 14(b). To understand the texture evolution related to different regions in a typical hot compressed specimen, CPFEM simulation was conducted at 1173 K and  $0.001 \text{ s}^{-1}$ . It could be observed that the uniform deformation zone

developed high plastic strain (location 1, see Figure 14(b)) as compared to other locations (locations 2 to 5, see Figure 14(b)). The simulated crystallographic texture corresponds to different regions in the hot compressed specimen (as illustrated in Figure 14(b)) is depicted in  $\varphi_2 = 0 \text{ deg}$  sections in Figures 14(c) through (g). The texture was stronger (MRD  $\sim 3.3$ , Figure 14(c)) in location 1 as compared to other locations (MRD  $\leq 2.5$ , Figures 14(d) through (g)) and it is attributed to the accumulation of larger plastic strain ( $\sim 1.2$ , Figure 14(b)) in the uniform deformation zone. To validate the simulated texture, the experimentally obtained texture from the deformed grains (grains with GOS  $\geq 1.5 \text{ deg}$ ) corresponding to these locations are also depicted in Figures 14(c') through (g'). It could be observed that the simulated texture showed a good agreement with the experimental observations (Figures 14(c) through (g) and c' through g') in this alloy. The  $\langle 011 \rangle // \text{ND}$  fiber (Figures 14(c') through (g') and Figure 11(a)) is evident in location 1 to 5 of hot compressed specimen which is also accurately predicted by the CPFEM simulation (Figures 14(c) through (g) and Figure 11(a)). Further, the simulated texture components obtained (from location 1, see Figure 14(b)) at different strain rates ( $0.001$  to  $10 \text{ s}^{-1}$ ) are represented in  $\varphi_2 = 0 \text{ deg}$  and  $\varphi_2 = 45 \text{ deg}$  sections of the ODF (Figures 15(a) through (c)). No significant variation in the evolution of texture components was noticed, though the texture intensity increased with the strain rate (MRD  $\sim 3.3$  to  $5.5$ , Figures 15(a) through (c)), as evident in the experimental ODF (MRD  $\sim 2.5$  to  $3.1$ , Figure 13(a)).

### 3. Texture evolution in recrystallized grains

The  $\varphi_2 = 0 \text{ deg}$  and  $\varphi_2 = 45 \text{ deg}$  section of the ODF corresponding to the DRX microstructures following deformation at 1173 K/ $10 \text{ s}^{-1}$  and 1273 K/ $0.1 \text{ s}^{-1}$  are illustrated in Figures 11(d) and (e). While the crystallographic texture has significantly weakened (MRD  $\sim 1.1$  to  $1.2$ , Figures 11(d) and (e)) as compared to the deformed grains (MRD  $\sim 3.5$ , Figure 11(c)), the deformation texture components are still persisted, particularly in the 1273 K/ $0.1 \text{ s}^{-1}$  condition (Figures 11(c) and (e)). The ND-IPF also shows a weak clustering (MRD  $\sim 1.1$ ) of orientation near  $\langle 011 \rangle$  direction (Figure 12(b)) similar to the deformed grains (Figure 12(a)). Weakly textured  $\langle 001 \rangle // \text{ND}$  fiber (MRD  $\sim 1.1$ ) was also evident in DRX grains (Figure 12(b)). Following deformation at 1273 K to 1323 K/ $0.001 \text{ s}^{-1}$ , the Cube and Rotated Cube components (Figure 11(f) and (g)) as well as  $\langle 111 \rangle // \text{RD}$  fiber slightly strengthened (MRD  $\sim 1.1$ , Figures 12c) as compared to fine DRX grains (Figures 11(d) and (e) and 12(b)). Moreover, a  $\langle 001 \rangle // \text{ND}$  fiber has been developed (Figures 11(h) through (k)) following deformation at temperatures 1373 K to 1423 K, and its strength has been increased (MRD  $\sim 1.4$  to  $5$ , Figures 11(h) through (k)) with the increase in DRX grain size ( $D_{\text{DRX}} \sim 5$  to  $33 \mu\text{m}$ , Figure 5(a)). The IPF also reveals the presence of strong  $\langle 001 \rangle // \text{ND}$  fiber (MRD  $\sim 3$ , Figure 12(d)) following deformation at  $0.001 \text{ s}^{-1}$ /1423 K.

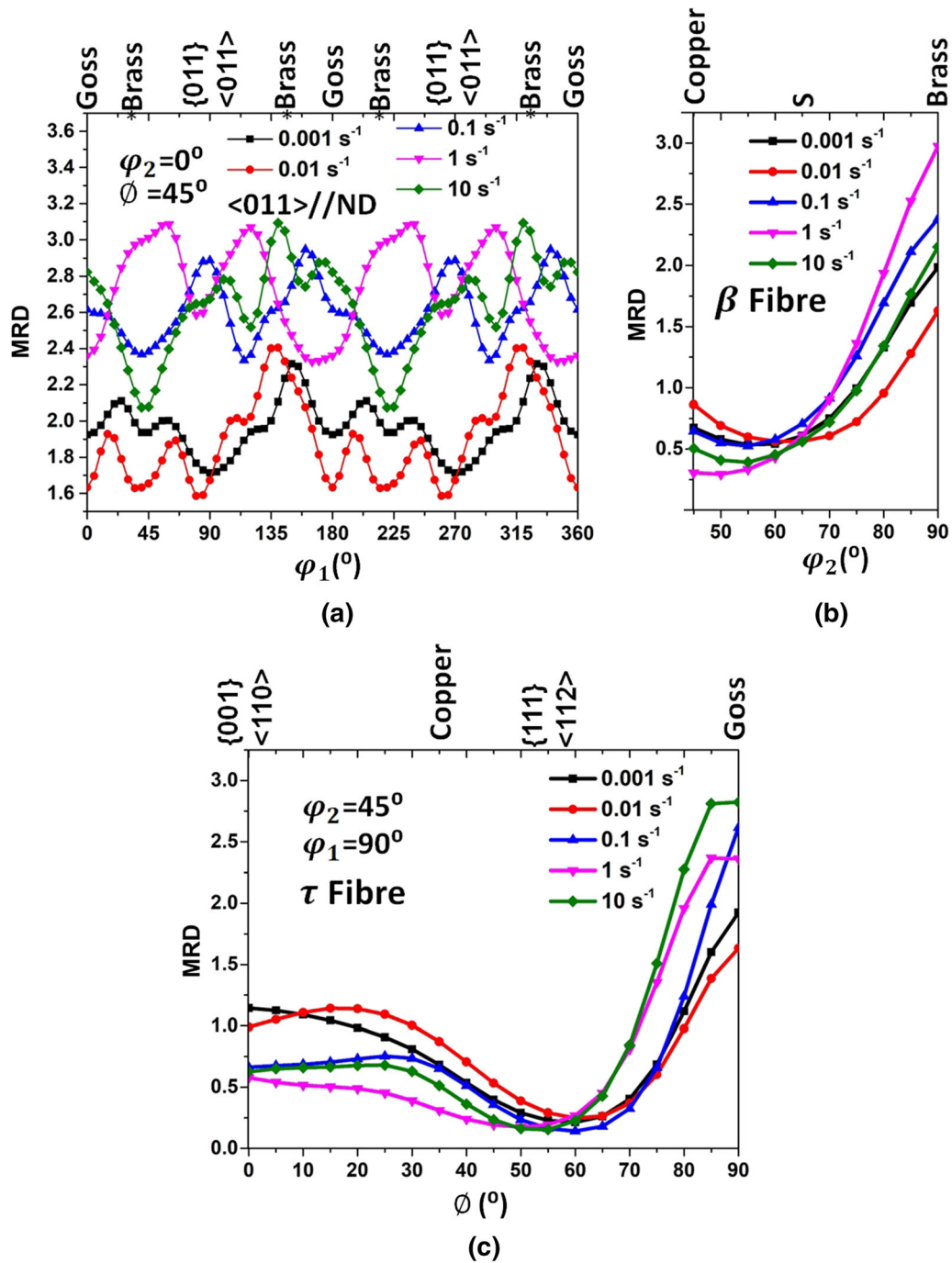


Fig. 13—The experimental texture intensities along (a)  $\langle 011 \rangle // ND$ , (b)  $\beta$ , (c)  $\tau$  fibers following deformation at 1173 K and strain rates 0.001 to  $10 \text{ s}^{-1}$ . The DRX grains ( $GOS < 1.5 \text{ deg}$ ) are omitted from the fiber texture evaluation.

#### 4. Overall fiber texture evolution

From the aforementioned results, it is observed that the texture evolution in the alloy was dependent on deformation temperature ( $T$ ) and strain rate ( $\dot{\epsilon}$ ). The  $\dot{\epsilon}$  and  $T$  could be combined to a single quantity known as Zener–Hollomon parameter ( $Z$ )<sup>[60]</sup>,

$$Z = \dot{\epsilon} \exp\left(\frac{Q}{RT}\right) \quad [8]$$

where  $Q$  activation energy for hot deformation ( $482 \text{ kJ mol}^{-1}$  in super austenitic stainless steel<sup>[2]</sup>). The

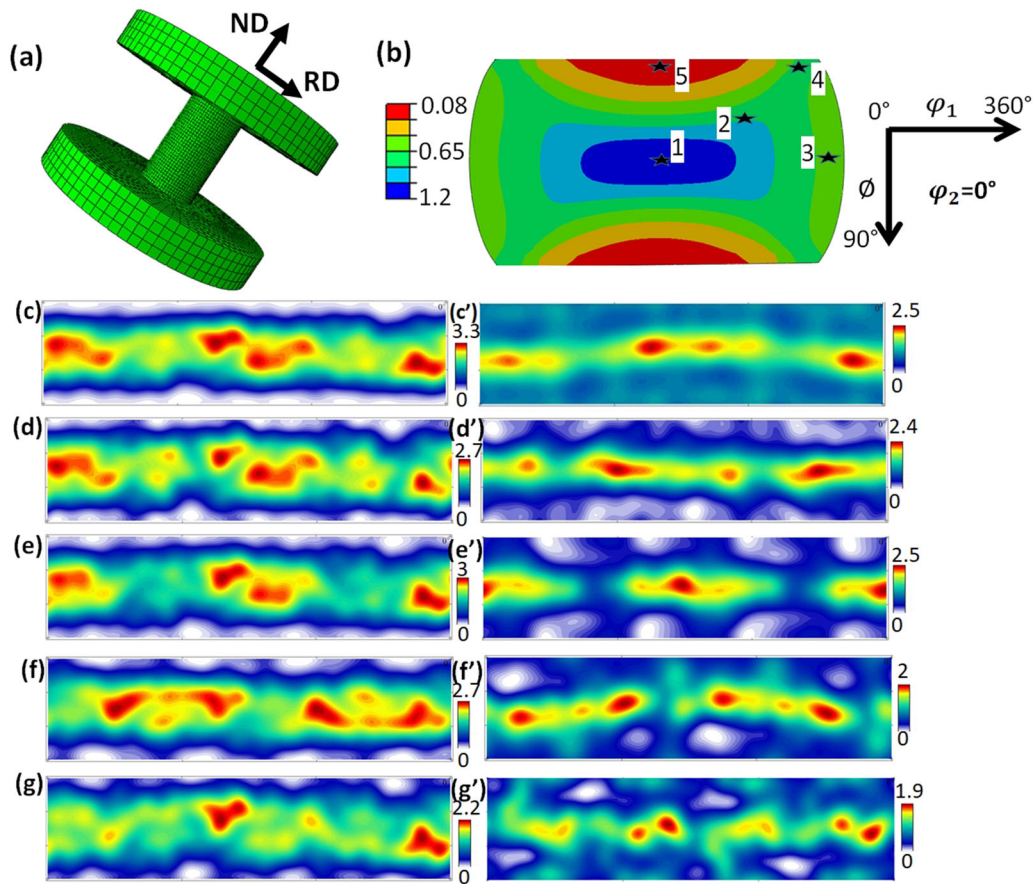


Fig. 14—(a) The schematic illustration of the compression specimen meshed with C3D8R-type elements, (b) the simulated equivalent plastic strain distribution associated with the RD-ND section of a deformed specimen (at 1173 K and  $0.001 \text{ s}^{-1}$ ). The (c through g) simulated and (c' through g') experimental ODF sections  $\varphi_2 = 0^\circ$  deg obtained from the different positions viz. (c and c') 1, (d and d') 2, (e and e') 3, (f and f') 4, and (g and g') 5, as marked in Fig. 14(b).

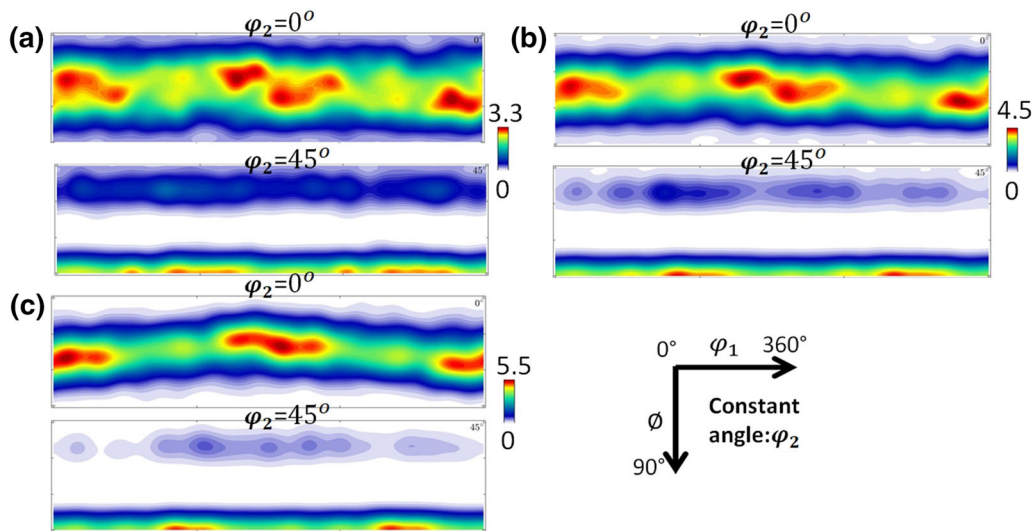


Fig. 15—The ODF sections ( $\varphi_2 = 0^\circ$  deg and  $45^\circ$  deg) simulated at 1173 K and strain rate (a)  $0.001$ , (b)  $0.1$ , (c)  $10 \text{ s}^{-1}$ .

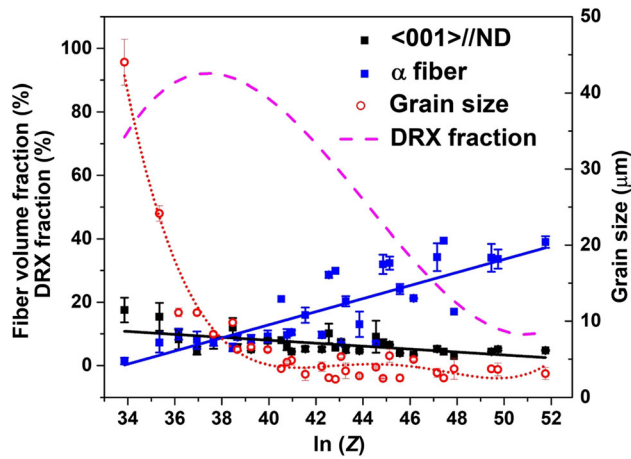


Fig. 16—The variation of the volume fraction of different fiber components, DRX fraction (pct) and grain size with respect to  $\ln(Z)$  following hot compression at temperatures 1173 K to 1423 K and strain rates 0.001 to  $10 \text{ s}^{-1}$ .

reported relationship between the  $Z$  and deformation parameters in the super austenitic stainless steel employed in this study could be expressed as,<sup>[2]</sup>

$$9.7 \times 10^{15} [\sinh(0.01\sigma_p)]^{3.1} = \dot{\epsilon} \exp\left(\frac{58013}{T}\right) = Z \quad [9]$$

where  $\sigma_p$  is the peak stress. The overall volume fraction of different fiber components such as  $\langle 011 \rangle // \text{ND}$  and  $\langle 001 \rangle // \text{ND}$  was evaluated and correlated with Zener–Hollomon parameter ( $Z$ ). It is observed that the volume fraction of  $\langle 011 \rangle // \text{ND}$  component ( $\alpha$  fiber) increased with an increase in Zener–Hollomon parameter (see Figure 16) following deformation whereas  $\langle 001 \rangle // \text{ND}$  exhibited the reverse trend. It is also interesting to note that the volume fraction of  $\langle 001 \rangle // \text{ND}$  component increased with an increase in the grain size (see dotted lines in Figure 16).

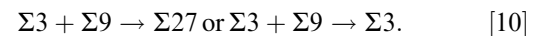
## IV. DISCUSSION

### A. $\Sigma 3$ Twin Boundary and TRD Evolution During DRX

The grain boundary map superimposed with color-coded grains of the specimen deformed at 1173 K– $10 \text{ s}^{-1}$  reveals the clear initiation of DRX (Figure 8). The pre-existing high-angle boundaries appear to be bulged (marked by red arrows in Figure 8) in some locations. It is well recognized that the bulging process due to SIBM results in the formation of DRX nuclei, which eventually grows by replacing the work-hardened grains,<sup>[23]</sup> The SIBM is often accompanied by twinning as reported in earlier studies.<sup>[20,27,28]</sup> Though few small DRX grains do not contain  $\Sigma 3$  boundaries (as shown by brown dotted arrows in Figure 8), the majority of the DRX grains contain  $\Sigma 3$  twin boundaries. Mahajan *et al.* have reported that twin boundaries are formed behind the migrating boundaries forming  $\{111\}$  steps on the

boundary.<sup>[61]</sup> Miura *et al.*<sup>[24]</sup> and Mandal *et al.*<sup>[20]</sup> have reported that twinning is an important mechanism during DRX. The fraction of  $\Sigma 3$  annealing twins increased with the DRX fraction in the present study (Figure 5(b) and 6) which is consistent with the previous results.<sup>[20,24,27]</sup> Further, the  $\Sigma 3$  twin boundary fraction increased exponentially with DRX grain size (Figure 7), while very less number of  $\Sigma 3$  twin boundaries were observed at the interface of deformed and DRX grains (Figure 8). These observations imply that the annealing twins were predominantly produced during the growth of DRX grains which accord with earlier studies.<sup>[24,28,29,36]</sup> It has been advocated that twin boundaries essentially formed due to growth accident.<sup>[28]</sup> To validate Pande’s model (as shown in Eq. [7]), the plot between TD and DRX grain size is illustrated in Figure 7. The variation between TD and DRX grain size essentially followed Pande’s model.<sup>[28]</sup> which substantiates that the growth accident is the primary mechanism for  $\Sigma 3$  boundary generation in the alloy. However, a scatter is persistent in Figure 7 (*i.e.*, TD vs  $D_{\text{DRX}}$ ) corresponding to the DRX grain diameter of  $\leq 5 \mu\text{m}$ . It could be associated with the limitations of Pande’s model, which does not consider the variation of the TD with temperature and strain rate following hot deformation.<sup>[25,29]</sup> Pande’s model, essentially a growth accident model, does not consider  $\Sigma 3$  twin boundary evolution during DRX nucleation<sup>[23]</sup> and  $\Sigma 3$  regeneration.<sup>[21,29]</sup>

It is well known that during  $\Sigma 3$  regeneration process,  $\Sigma 3$  boundaries interact with  $\Sigma 3$  boundaries to form  $\Sigma 9$  boundaries.<sup>[21]</sup> Similarly,  $\Sigma 9$  boundaries interact with  $\Sigma 3$  boundaries to form  $\Sigma 3$  boundaries or  $\Sigma 27$  boundaries.<sup>[21]</sup> This process could be represented as follows,



Essentially, when a  $\Sigma 3$  boundary meets with a  $\Sigma 9$  boundary, a new  $\Sigma 27$  boundary or  $\Sigma 3$  boundary could be generated which forms a triple junction. In this regard, the combined fraction of  $\Sigma 9$  and  $\Sigma 27$  could represent the extent of  $\Sigma 3$  regeneration.<sup>[21]</sup> It is observed that the fraction of  $\Sigma 9 + \Sigma 27$  boundaries ( $\sim 0.03$ ) was slightly higher following deformation at 1323 K/ $0.001 \text{ s}^{-1}$  as compared to other domains (Figure 6). This observation hints the occurrence of perceptible  $\Sigma 3$  regeneration in the domain 1323 K/ $0.001 \text{ s}^{-1}$ .<sup>[25]</sup> Conversely, Mandal *et al.*<sup>[20]</sup> have pointed out that the marginal increase in the fraction of  $\Sigma 9 + \Sigma 27$  boundaries ( $\sim 0.03$ , Figure 6) may not be significant enough to substantiate frequent  $\Sigma 3$  regeneration following hot deformation. In this context, to identify the extent of  $\Sigma 3$  regeneration, TRD analyses were performed. A recent study has reported that TRD analysis is effective in understanding the extent of multiple twinning or  $\Sigma 3$  regeneration.<sup>[62]</sup> Similarly, the statistical parameters such as  $N_{\text{TRD}}$  and average LLCs could also reveal how frequently the multiple twinning occurred following deformation.<sup>[31]</sup> The values of  $N_{\text{TRD}}$  ( $\sim 5$ ) and average LLCs ( $\sim 0.7$ ) were found to be reasonably higher at 1323 K/ $0.001 \text{ s}^{-1}$  (Figure 9), and

relatively larger TRDs were formed (Figure 10(f)). This essentially further confirms the perceptible occurrence of multiple twinning in this condition.<sup>[32]</sup> On the other hand,  $N_{\text{TRD}} (< 2)$  and average LLC (0.3 to 0.4) were found to be lower at 1423 K/1 to 10 s<sup>-1</sup> though the domain is associated with a higher  $\sum 3$  boundary fraction (~ 0.32, Figure 6). Relatively smaller grain size ( $\leq 6 \mu\text{m}$ , Figure 5(a)) was obtained in this domain which refers to higher nucleation rate.<sup>[12]</sup> Liu *et al.*<sup>[63]</sup> have also documented that a high nucleation rate increases the TD, but reduces the TRD size. Due to the high nucleation rate and fine grain sizes ( $\leq 6 \mu\text{m}$ , Figure 5(a)), the density of the RHABs is expected to be higher which restrict the effective  $\sum 3$  boundary interaction to form large TRD networks.<sup>[63]</sup> Following deformation at  $\sim 0.001 \text{ s}^{-1}/1373 \text{ K}$  to 1423 K, rapid grain growth occurred (Figure 3(h)) and the TRD size became larger (Figure 10(g)). However, the  $\sum 3$  regeneration process was not significant to form large TRD networks with higher  $N_{\text{TRD}}$  in this domain. This is probably due to the grain coarsening phenomenon and low twin density (Figure 7) as suggested in previous studies.<sup>[63]</sup>

From the above discussion, it is apparent that large TRD networks with high  $N_{\text{TRD}}$  and high average LLC (Figure 9) were not formed in both the fine (1423 K/1 to 10 s<sup>-1</sup>) and coarse-grained ( $\sim 0.001 \text{ s}^{-1}/1373 \text{ K}$  to 1423 K) microstructures. However, it is expected that grain sizes, falling in the range of  $\sum 3$  regeneration domain (*i.e.*, 1323 K/0.001 s<sup>-1</sup>,  $D_{\text{DRX}} \sim 9 \mu\text{m}$ , see Figure 5(a)), could yield relatively larger TRD networks. Interestingly, following deformation at  $\sim 1423 \text{ K}/0.1 \text{ s}^{-1}$ , the grain size was comparable to that of  $\sum 3$  regeneration domain ( $D_{\text{DRX}} \sim 9 \mu\text{m}$ , Figure 5(a)) but the TRD size was small (Figure 10(h)). Hence, it appears that the grain size is not the only factor that controls the TRD formation in the alloy during DRX. The observation is consistent with the proposal of Irukuvarghula *et al.*<sup>[30]</sup> that optimum temperature and strain rate are essential for TRD development during recrystallization.

## B. Texture Changes Following Hot Deformation

The AR microstructure reveals the presence of weak near Brass and near  $\{120\} \langle 001 \rangle$  components (Figure 11(b)) and these are generally observed in low SFE energy materials during recrystallization.<sup>[38,64]</sup> From the analysis of texture results, it is evident that the crystallographic textures in deformed grains and DRX grains are different, and these are discussed below.

### 1. Evolution of deformation texture

Following deformation at 1173 K/10 s<sup>-1</sup>, the ODF  $\varphi_2 = 0 \text{ deg}$  and  $\varphi_2 = 45 \text{ deg}$  (Figure 11(c)) and ND-IPF (Figure 12(a)) exhibits strong clustering of orientations near  $\langle 011 \rangle // \text{ND}$ , revealing the formation of  $\langle 011 \rangle // \text{ND}$  fiber ( $\alpha$  fiber) in the deformed grains.<sup>[39]</sup> It is well known that the formation of  $\alpha$  fiber is associated with shear deformation in FCC material.<sup>[39]</sup> The Brass and Goss orientations (which is associated with  $\alpha$  fiber, Figure 13(a)) were stronger, where the Copper and S orientations (associated with the  $\alpha$  fiber, Figure 13(b))

were relatively weaker in the alloy. Several researchers have suggested that the formation of different components in  $\alpha$  fiber depends on SFE,<sup>[57]</sup> non-octahedral slip,<sup>[39,65]</sup> the extent of deformation twinning,<sup>[66]</sup> shear band formation<sup>[67]</sup> *etc.*

Further, the volume fraction of  $\langle 011 \rangle // \text{ND}$  fiber ( $\alpha$  fiber) in both the deformed and DRX grains were evaluated and correlated with the  $Z$  (Figure 16). The volume fraction of  $\langle 011 \rangle // \text{ND}$  fiber decreased with the decrease in  $Z$ . The deformation texture annihilated following DRX (Figures 11c and d) which is consistent with the observed decrease in  $\langle 011 \rangle // \text{ND}$  fiber with the decrease in  $Z$  (Figure 16). Moreover, the increase in strain rate at 1173 K (or increase in  $Z$ ) has also strengthened the intensity of  $\langle 011 \rangle // \text{ND}$  deformed grains (Figure 13(a)). The strengthening of texture at higher strain rate could be explained based on the number of active slip systems operating at higher strain rates (or at higher  $Z$ ). The crystallographic texture evolution is decided by lattice spin ( $\underline{\underline{\dot{\Omega}}}$ ) which is correlated to the amount of rigid body rotation ( $\underline{\underline{\dot{\beta}}}$ ) and plastic spin ( $\underline{\underline{\dot{\psi}}}$ ) as follows,<sup>[68–70]</sup>

$$\underline{\underline{\dot{\Omega}}} = \underline{\underline{\dot{\beta}}} - \underline{\underline{\dot{\psi}}} \quad [11]$$

For uniaxial compression, the rigid body rotation is zero ( $\underline{\underline{\dot{\beta}}} = 0$ )<sup>[69]</sup> and hence the plastic spin dictates the texture evolution (see Eq. 11). Canova *et al.*<sup>[71]</sup> have reported that the lower plastic spin is often associated with the high strain rate sensitivity and activation of more number of slip systems. Texture strengthening (Figure 13(a)) (or high lattice spin) and lower strain rate sensitivity ( $m \sim 0.0025$ , Table II) at higher strain rates could be associated with the decrease in the number of active slip systems (or high plastic spin) at higher strain rates. In addition to this, CPFEM simulation indicated that the plastic strain developed at the uniform deformation zone increased with the increase in strain rate (1.2 to 1.5). The increase in plastic strain also led to the higher texture strengthening at higher strain rate (or high  $Z$  at constant temperature).

The strain path diagram is illustrated in Figure 17(a) which shows the variation of major strain or in-plane maximum principal strain,  $\epsilon_{\text{max}}$  with the variation of minor strain or in-plane minimum principal strain,  $\epsilon_{\text{min}}$ . In the case of pure shear, the slope  $n'$  (*i.e.*  $\frac{\epsilon_{\text{max}}}{\epsilon_{\text{min}}}$ ) yields  $-1$  while uniaxial compression  $n'$  yields  $-0.5$ .<sup>[72]</sup> It is observed that locations 1 to 2 (refer Figure 14(b)) exhibited uniaxial compression while location 3 slightly deviated away from the uniaxial towards the plane strain compression (Figure 17(a)). Meanwhile, location 3 is identified by the lower value of von Mises stress which also indicates the shift from uniaxial to multi-axial deformation condition (Figure 17(b)). While the peak intensity in the experimental ODF at location 3 (Figure 14(e')) indicates a slight shift towards Goss orientation, the simulated ODF essentially did not

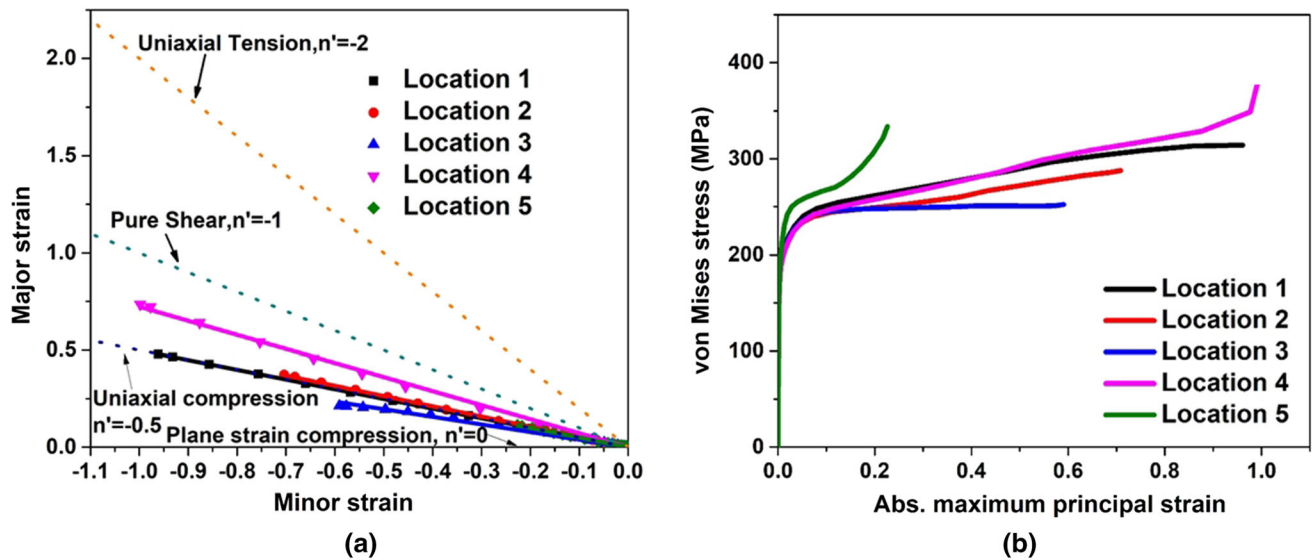


Fig. 17—The variation of (a) major strain and minor strain, (b) von Mises stress vs. absolute maximum principal strain in the deformed specimen at different locations (1 to 5) in Fig. 14(b) as obtained through CPFEM simulation at 1173 K and  $0.001 \text{ s}^{-1}$ .

indicate a substantial variation in the texture distribution along  $\alpha$  fiber (Figure 14(e)). Further, the  $\varepsilon_{\max}$  vs  $\varepsilon_{\min}$  diagram corresponding to location 4 indicates a deviation towards pure shear condition (Figure 17(a)). Following deformation, in case of pure shear, the rigid body rotation should be equal to plastic spin (Eq. [11]) for attaining a stable orientation.<sup>[69]</sup> This criterion is achieved only when two slip systems are operational.<sup>[73]</sup> Activation of more number of slip systems would result in a stable texture if rigid body rotation counteract the plastic spin.<sup>[69]</sup> The rigid body rotation is manifested in the  $\varphi_2 = 0$  deg section of the ODF as a shift in maximum intensity along  $\varphi_1$  direction (Figures 14(f) and (f')). Similar variation in texture intensity along  $\varphi_1$  is previously reported in pure torsion also.<sup>[69,73–75]</sup> Furthermore, the texture evolution in location 5 (Figures 14(g) and (g')) was relatively lower (MRD  $\sim 1.9$ ) due to the lower plastic strain (Figure 14(b)).

## 2. Recrystallization texture development

The evolution of fine ( $D_{\text{DRX}} \leq 3 \mu\text{m}$ , Figure 5(a)) and equiaxed (Figures 3(b) through (d)) DRX grains are evident following deformation at 0.1 to  $10 \text{ s}^{-1}/1173 \text{ K}$  to  $1273 \text{ K}$ . In these conditions, the DRX texture was almost random consisting of weak-deformation components as seen in Figures 11(d) and (e). During DRX activity, small DRX nuclei initially formed at serrated boundaries via grain boundary bulging process (Figure 8).<sup>[24]</sup> Following the DRX nucleation, the grain boundaries continue to migrate thus consuming the deformed grains accompanied by twinning.<sup>[24]</sup> In copper bi-crystals, Horton *et al.*<sup>[76]</sup> have observed that such twinning during SIBM could potentially weaken the texture. Following deformation at high temperatures ( $\geq 1373 \text{ K}$ ), cube-oriented grains were part of the  $\langle 001 \rangle$  fiber (Figures 11(h) and (k)) which is considered as the preferred orientation for nucleation and growth following static recrystallization in FCC alloys.<sup>[77,78]</sup>

Additionally, weak clustering of  $\{110\} \langle 111 \rangle$  and  $\{110\} \langle 112 \rangle$  orientations are also observed in the ODF  $\varphi_2 = 0$  deg sections (Figures 11(g) and (i)). Hutchinson has recorded that the solute drag effect of Mn and P (which is present in the super austenitic stainless steel, see Table 1) could cause preferential DRX nucleation with  $\langle 111 \rangle$  component which leads to the formation of this typical texture component.<sup>[79]</sup>

It is interesting to note that the texture was relatively weaker following deformation at  $1323 \text{ K}/0.001 \text{ s}^{-1}$  (MRD  $\sim 1.4$ , Figure 11(g)) as compared to the condition  $\sim 1423 \text{ K}/0.1 \text{ s}^{-1}$  (MRD  $\sim 2.5$ , Figure 11(j)), though both the conditions reveal the similar grain sizes ( $D_{\text{DRX}} \sim 9 \mu\text{m}$ , Figure 5(a)). As both the grain sizes are comparable, the texture convergence associated with the condition  $\sim 1423 \text{ K}/0.1 \text{ s}^{-1}$  could not be related to the difference in the grain sizes. It is noted that texture convergence could not be associated with crystallographic slip<sup>[67]</sup> in a typical high DRX domain ( $> 80$  pct, Figure 5(b)). Moreover, the condition  $\sim 1323 \text{ K}/0.001 \text{ s}^{-1}$  reveals bigger TRDs (Figure 10(f)) while the domain  $\sim 1423 \text{ K}/0.1 \text{ s}^{-1}$  is identified by relatively smaller TRDs (Figure 10(h)). It is reported that the large TRDs are formed in the microstructure due to multiple twinning.<sup>[31]</sup> During this process, new  $\Sigma 3$  and  $\Sigma 9$  boundaries are also formed which changes crystallographic orientations.<sup>[80,81]</sup> The new orientations being introduced by the repeated twinning process<sup>[80,81]</sup> counteract the texture convergence during grain growth. These processes are believed to be associated with texture weakening as evident in the domain  $\sim 1323 \text{ K}/0.001 \text{ s}^{-1}$ .

From the above analysis, we conclude that the texture changes in the studied alloy is associated with resistance to deformation, strain path, the extent of DRX, and the formation of TRDs following hot deformation. Moreover, we observed the formation of relatively large TRDs at  $1323 \text{ K}/0.001 \text{ s}^{-1}$  which led to texture

randomization following hot deformation. However, large TRDs were not observed in the other deformation conditions in where the growth accident was the major  $\Sigma 3$  twin boundary evolution mechanism.

## V. CONCLUSIONS

The microstructure and texture of super austenitic stainless steel hot compressed at various temperatures (1173 K to 1423 K) and strain rates (0.001 to 10 s<sup>-1</sup>) has been investigated employing electron backscattered diffraction. The evolution of  $\Sigma 3$  twin boundaries following hot deformation has been quantified based on twin density and twin-related domains (TRDs) analyses. The deformation texture has also been simulated at various regions of a typical hot compressed specimen. The following significant conclusions are derived from this study.

1. Strong  $\langle 011 \rangle // \text{ND}$  fiber (or  $\alpha$  fiber) texture developed in the deformed grains following deformation at 1173 K/0.001 to 10 s<sup>-1</sup>. The volume fraction of  $\langle 011 \rangle // \text{ND}$  decreased significantly with the decrease in resistance to deformation. The other fibers such as  $\beta$  and  $\tau$  were not strengthened following hot compression.
2. The DRX activity at 1173 K to 1273 K and 0.1 to 10 s<sup>-1</sup> led to the formation of fine and equiaxed DRX grains ( $\leq 3 \mu\text{m}$ ) with near-random texture in this alloy. Following deformation at temperatures 1373 K to 1423 K and strain rates 0.001 to 0.01 s<sup>-1</sup>, the strengthening of  $\langle 100 \rangle // \text{ND}$  fiber was observed, which is found to be associated with grain growth.
3. The deformation texture at different regions of a typical hot compressed specimen was evaluated employing the crystal plasticity finite element method (CPFEM) considering octahedral slip. A  $\langle 011 \rangle // \text{ND}$  fiber evolved in different regions investigated in the compressed specimen. The relative intensity of the individual texture components varied according to the different strain paths at different locations in the compressed specimen.
4. The TRDs analyses revealed that the  $\Sigma 3$  regeneration mechanism is insignificant over the whole range of strain rates and temperatures. The growth accident was the primary  $\Sigma 3$  twin boundary evolution mechanism in this alloy. However, the occurrence of  $\Sigma 3$  regeneration also noticed in a small domain of hot working ( $\sim 1323 \text{ K}/0.001 \text{ s}^{-1}$ ) which led to texture randomization and formation of relatively larger TRDs in the microstructure.

## ACKNOWLEDGMENTS

The authors are indebted to C. Cayron for providing us the ARPGE software for the TRD analysis. We are also thankful to Q. Ma and E.B. Marin for

developing Abaqus® CPFEM code<sup>[49]</sup> which is used in the present analyses.

## REFERENCES

1. A. Mirzaei, A. Zarei-Hanzaki, and H.R. Abedi: *Metall. Mater. Trans. A*, 2016, vol. 47A, pp. 2037–48.
2. K. Arun Babu, S. Mandal, C.N. Athreya, B. Shakthipriya, and V.S. Sarma: *Mater. Des.*, 2017, vol. 115, pp. 262–75.
3. N. Rajendran and S. Rajeswari: *J. Mater. Sci.*, 1996, vol. 31, pp. 6615–19.
4. J. Moon, T.-H. Lee, C.-H. Lee, S.-J. Park, J.-H. Shin, and J.-W. Lee: *Metall. Mater. Trans. A*, 2019, vol. 50A, pp. 5670–77.
5. C. Gupta, J.S. Jha, B. Jayabalan, R. Gujrati, A. Alankar, and S. Mishra: *Metall. Mater. Trans. A*, 2019, vol. 50A, pp. 4714–31.
6. R.D. Doherty, D.A. Hughes, F.J. Humphreys, J.J. Jonas, D. Juul Jensen, M.E. Kassner, W.E. King, T.R. McNelley, H.J. McQueen, and A.D. Rollett: *Mater. Sci. Eng. A*, 1997, vol. 238, pp. 219–74.
7. D.-X. Wen, Y.C. Lin, X.-H. Li, and S.K. Singh: *J. Alloys Compd.*, 2018, vol. 764, pp. 1008–20.
8. Y.C. Lin, J. Huang, D.-G. He, X.-Y. Zhang, Q. Wu, L.-H. Wang, C. Chen, and K.-C. Zhou: *J. Alloys Compd.*, 2019, vol. 795, pp. 471–82.
9. K. Arun Babu and S. Mandal: *Mater. Sci. Eng. A*, 2017, vol. 703, pp. 187–95.
10. N.S. Shah, S. Sunil, and A. Sarkar: *Metall. Mater. Trans. A*, 2018, vol. 49A, pp. 2644–53.
11. S. Roy, S. Biswas, K. Arun Babu, and S. Mandal: *J. Mater. Eng. Perform.*, 2018, vol. 27, pp. 3762–72.
12. S. Mandal, M. Jayalakshmi, A.K. Bhaduri, and V.S. Sarma: *Metall. Mater. Trans. A*, 2014, vol. 45A, pp. 5645–56.
13. D. Samantaray, S. Mandal, M. Jayalakshmi, C.N. Athreya, A.K. Bhaduri, and V.S. Sarma: *Mater. Sci. Eng. A*, 2014, vol. 598, pp. 368–75.
14. N. Haghdadadi, P. Cizek, H. Beladi, and P.D. Hodgson: *Acta Mater.*, 2017, vol. 126, pp. 44–57.
15. S. Mandal, A.K. Bhaduri, and V.S. Sarma: *Metall. Mater. Trans. A*, 2012, vol. 43A, pp. 410–14.
16. A. Dehghan-Manshadi and P.D. Hodgson: *Metall. Mater. Trans. A*, 2008, vol. 39A, pp. 2830–40.
17. A. Chatterjee, A. Dutta, S.M. Basiruddin, R. Mitra, A.K. Bhaduri, and D. Chakrabarti: *Metall. Mater. Trans. A*, 2017, vol. 48A, pp. 2410–24.
18. K. Arun Babu, Y.H. Mozumder, R. Saha, V.S. Sarma, and S. Mandal: *Mater. Sci. Eng. A*, 2018, vol. 734, pp. 269–80.
19. Y.H. Mozumder, K. Arun Babu, R. Saha, and S. Mandal: *Mater. Charact.*, 2018, vol. 146, pp. 1–14.
20. S. Mandal, A.K. Bhaduri, and V.S. Sarma: *Metall. Mater. Trans. A*, 2012, vol. 43A, pp. 2056–68.
21. V. Randle: *Mater. Sci. Technol.*, 2010, vol. 26, pp. 253–61.
22. D. An, T.A. Griffiths, P. Konijnenberg, S. Mandal, Z. Wang, and S. Zaeferrer: *Acta Mater.*, 2018, vol. 1, pp. 297–307.
23. E. Brünger, X. Wang, and G. Gottstein: *Scr. Mater.*, 1998, vol. 38, pp. 1843–49.
24. H. Miura, T. Sakai, R. Mogawa, and G. Gottstein: *Scr. Mater.*, 2004, vol. 51, pp. 671–75.
25. M. Detrois, R.L. Goetz, R.C. Helmink, and S. Tin: *Mater. Sci. Eng. A*, 2015, vol. 647, pp. 157–62.
26. H. Gleiter: *Acta Metall.*, 1969, vol. 17, pp. 1421–28.
27. S.K. Pradhan, S. Mandal, C.N. Athreya, K. Arun Babu, B. de Boer, and V.S. Sarma: *Mater. Sci. Eng. A*, 2017, vol. 700, pp. 49–58.
28. C.S. Pande, M.A. Imam, and B.B. Rath: *Metall. Trans. A*, 1990, vol. 21A, pp. 2891–96.
29. B.R. Chen, A.C. Yeh, and J.W. Yeh: *Sci. Rep.*, 2016, vol. 6, pp. 1–9.
30. S. Irukuvarghula, H. Hassanin, C. Cayron, M.M. Attallah, D. Stewart, and M. Preuss: *Acta Mater.*, 2017, vol. 133, pp. 269–81.
31. J. Lind, S.F. Li, and M. Kumar: *Acta Mater.*, 2016, vol. 114, pp. 43–53.



32. T.S. Prithiv, P. Bhuyan, S.K. Pradhan, V.S. Sarma, and S. Mandal: *Acta Mater.*, 2018, vol. 146, pp. 187–201.
33. T. Watanabe and S. Tsurekawa: *Acta Mater.*, 1999, vol. 47, pp. 4171–85.
34. S.K. Pradhan, P. Bhuyan, C. Kaithwas, and S. Mandal: *Metall. Mater. Trans. A*, 2018, vol. 49A, pp. 2817–31.
35. C.K. Kaithwas, P. Bhuyan, S.K. Pradhan, and S. Mandal: *Mater. Charact.*, 2018, vol. 145, pp. 582–93.
36. H. Beladi, P. Cizek, and P.D. Hodgson: *Metall. Mater. Trans. A*, 2009, vol. 40A, pp. 1175–89.
37. N. Eftekhari, A. Zarei-Hanzaki, A. Shamsolhodaei, A.-L. Helbert, and T. Baudin: *Adv. Eng. Mater.*, 2018, vol. 20, pp. 1438–56.
38. M. Rout, S. Biswas, R. Ranjan, S.K. Pal, and S.B. Singh: *Metall. Mater. Trans. A*, 2017, vol. 49A, pp. 864–80.
39. D. Raabe: *Acta Mater.*, 1997, vol. 45, pp. 1137–51.
40. S. Li, Q. Zhao, Z. Liu, and F. Li: *J. Mater. Eng. Perform.*, 2018, vol. 27, pp. 3350–73.
41. N.P. Gurao, R. Kapoor, and S. Suwas: *Metall. Mater. Trans. A*, 2010, vol. 41A, pp. 2794–804.
42. A. Dehghan-Manshadi, M.R. Barnett, and P.D. Hodgson: *Metall. Mater. Trans. A*, 2008, vol. 39A, pp. 1359–70.
43. G.B. Sarma and P.R. Dawson: *Acta Mater.*, 1996, vol. 44, pp. 1937–53.
44. S.R. Kalidindi, C.A. Bronkhorst, and L. Anand: *J. Mech. Phys. Solids*, 1992, vol. 40, pp. 537–69.
45. A.J. Beaudoin, P.R. Dawson, K.K. Mathur, and U.F. Kocks: *Int. J. Plasticity*, 1995, vol. 11, pp. 501–21.
46. P. Van Houtte, S. Li, M. Seefeldt, and L. Delannay: *Int. J. Plasticity*, 2005, vol. 21, pp. 589–624.
47. V.M. Miller, S.L. Semiatin, C. Szczepanski, and A.L. Pilchak: *Metall. Mater. Trans. A*, 2018, vol. 49A, pp. 3624–36.
48. N.P. Gurao, P. Kumar, A. Sarkar, H.-G. Brokmeier, and S. Suwas: *J. Mater. Eng. Perform.*, 2013, vol. 22, pp. 1004–09.
49. E.B. Marin: *On the Formulation of a Crystal Plasticity Model*, Sandia National Laboratories, Livermore, 2006.
50. B. Bacroix and J.J. Jonas: *Textures Microstruct.*, 1988, vols. 8–9, pp. 267–311.
51. D. Raabe, D. Ma, and F. Roters: *Acta Mater.*, 2007, vol. 55, pp. 4567–83.
52. M. Liu, C. Lu, and A.K. Tieu: *Int. J. Solids Struct.*, 2015, vol. 54, pp. 42–49.
53. D. Raabe, Z. Zhao, and F. Roters: *Ser. Mater.*, 2004, vol. 50, pp. 1085–90.
54. D. Samantaray, S. Mandal, and A.K. Bhaduri: *Mater. Des.*, 2011, vol. 32, pp. 2797–802.
55. Y. Jin, M. Bernacki, G.S. Rohrer, A.D. Rollett, B. Lin, and N. Bozzolo: *Mater. Sci. Forum*, 2013, vol. 753, pp. 113–16.
56. C. Cayron: *J. Appl. Crystallogr.*, 2007, vol. 40, pp. 1183–88.
57. T. Leffers and R.K. Ray: *Prog. Mater. Sci.*, 2009, vol. 54, pp. 351–96.
58. P. Acar, A. Ramazani, and V. Sundararaghavan: *Metals (Basel)*, 2017, vol. 7, pp. 459–72.
59. M. Detrois, R.L. Goetz, R.C. Helmink, and S. Tin: *J. Mater. Sci.*, 2016, vol. 51, pp. 5122–38.
60. C. Zener and J.H. Hollomon: *J. Appl. Phys.*, 1944, vol. 15, pp. 22–32.
61. S. Mahajan, C.S. Pande, M.A. Imam, and B.B. Rath: *Acta Mater.*, 1997, vol. 45, pp. 2633–38.
62. C. Cayron: *Acta Crystallogr. A*, 2007, vol. 63, pp. 11–29.
63. T. Liu, S. Xia, H. Li, B. Zhou, Q. Bai, C. Su, and Z. Cai: *J. Mater. Res.*, 2013, vol. 28, pp. 1165–76.
64. P.P. Bhattacharjee, R.K. Ray, and N. Tsuji: *Metall. Mater. Trans. A*, 2010, vol. 41A, pp. 2856–70.
65. C. Maurice and J.H. Driver: *Acta Mater.*, 1997, vol. 45, pp. 4627–38.
66. H. Hu and R.S. Cline: *Textures Microstruct.*, 1988, vols. 8–9, pp. 191–206.
67. S.G. Chowdhury, S. Das, and P.K. De: *Acta Mater.*, 2005, vol. 53, pp. 3951–59.
68. R. Sonkusare, R. Jain, K. Biswas, V. Parameswaran, and N.P. Gurao: *J. Alloys Compd.*, 2020, vol. 823, p. 153763.
69. L.S. Tóth: A. Haldar, S. Suwas, and D. Bhattacharjee, eds., *Microstructure and Texture in Steels*, Springer London, London, 2009, pp. 225–46.
70. N.P. Gurao, S. Sethuraman, and S. Suwas: *Mater. Sci. Eng. A*, 2011, vol. 528, pp. 7739–50.
71. G.R. Canova, C. Fressengeas, A. Molinari, and U.F. Kocks: *Acta Metall.*, 1988, vol. 36, pp. 1961–70.
72. S.K. Paul, G. Manikandan, and R.K. Verma: *J. Strain Anal. Eng. Des.*, 2013, vol. 48, pp. 386–94.
73. L.S. Tóth, J.J. Jonas, D. Daniel, and J.A. Bailey: *Textures Microstruct.*, 1992, vol. 19, pp. 245–62.
74. S. Wroński, K. Wierzbanowski, B. Bacroix, T. Chauveau, M. Wróbel, A. Rauch, F. Montheillet, and M. Wroński: *Arch. Metall. Mater.*, 2009, vol. 54, pp. 89–102.
75. S. Suwas and A.K. Singh: *Mater. Sci. Eng. A*, 2003, vol. 356, pp. 368–71.
76. D. Horton, C.B. Thomson, and V. Randle: *Mater. Sci. Eng. A*, 1995, vol. 203, pp. 408–14.
77. O. Engler, H.E. Vatne, and E. Nes: *Mater. Sci. Eng. A*, 1996, vol. 205, pp. 187–98.
78. P. Dolzhenko, M. Tikhonova, R. Kaibyshev, and A. Belyakov: *Metals (Basel)*, 2019, vol. 9, pp. 30–42.
79. W.B. Hutchinson: *Int. Met. Rev.*, 1984, vol. 29, pp. 25–42.
80. G. Gottstein: *Acta Metall.*, 1984, vol. 32, pp. 1117–38.
81. V.Y. Gertsman, R.Z. Valiev, V.N. Danilenko, and O.V. Mishin: *Le J. Phys. Colloq.*, 1990, vol. 51, pp. C1–151–54.

**Publisher's Note** Springer Nature remains neutral with regard to jurisdictional claims in published maps and institutional affiliations.